PCCP

PAPER

View Article Online
View Journal | View Issue

Check for updates

Cite this: *Phys. Chem. Chem. Phys.*, 2026, **28**, 4485

Molecular wiring of chlorophyll *a* and cytochrome *c* on carbon black for amplified photocurrent generation and ROS profiling in cancer cells

Jayaprakash Meena,[ab] Sugumar Monisha,[ab] Tamizhselvi Ramasamy,[c] Kandhan Palanisamy,[d] Varatharaj Rajapandian,[e] K. Santhakumar*[b] and Annamalai Senthil Kumar*[ab]

Received 11th November 2025,
Accepted 11th January 2026

DOI: 10.1039/d5cp04355g

rsc.li/pccp

Natural processes like photosynthesis involve complex electron transfer pathways, including both direct electron transfer (DET) and molecular wiring, which are essential for biological energy conversion and storage. Replicating such systems in artificial platforms remains a major scientific challenge. In this study, we successfully fabricated a bioelectrode comprising chlorophyll, specifically plant-derived chlorophyll *a* (Chl*a*), molecularly wired with cytochrome *c* (Cytc) on a carbon black (CB)-modified electrode surface. This hybrid electrode, designated as CB@Cytc–Chl*a*, was prepared using a simple solution-phase approach. The system demonstrated efficient DET between the protein ensemble and the electrode surface. Cyclic voltammetry in nitrogen-purged pH 7 phosphate buffer revealed a well-defined and reversible redox couple at $E^\circ = -0.2$ V *vs.* Ag/AgCl, with a surface coverage value of 2.96 nmol cm^{-2}. Control experiments using electrodes modified with individual proteins (Cytc or Chl*a* alone) showed no such redox behavior, highlighting the importance of molecular wiring in the composite assembly. To probe specific interactions between Chl*a* and Cytc, *in situ* electrochemical quartz crystal microbalance (EQCM) analysis was performed, confirming strong binding affinity. Furthermore, *in situ* scanning electrochemical microscopy (SECM) in feedback mode revealed distinct electroactive sites on the bioelectrode surface. Under simulated solar illumination, the CB@Cytc–Chl*a* bioelectrode produced a significantly enhanced photocurrent compared to the control electrodes with individual components, indicating effective photo-induced charge transfer. The selective electrochemical reduction of hydrogen peroxide (H_2O_2) was explored as a model reaction at neutral pH, where the hybrid bioelectrode exhibited the highest current response relative to the protein-only modified electrodes. As a demonstration of practical utility, a selective batch-injection analysis of H_2O_2 was carried out using a three-in-one disposable screen-printed electrode modified with the CB@Cytc–Chl*a* composite. This system, integrated with a prototype wireless device, enabled sensitive one-drop detection of reactive oxygen species (ROS) released from chemically stressed cancer cells.

1. Introduction

Photosynthesis, the fundamental biological process through which plants convert solar energy into chemical energy, has long inspired the design of bio-mimetic energy systems.[1] Among the key components of this process is chlorophyll a (Chl*a*), a large pigment complex embedded in the thylakoid membranes of higher plants.[2] Chl*a* plays a critical role in the light-dependent reactions of photosynthesis by promoting the excitation of an electron from a specialized chlorophyll dimer, P700, to a terminal iron–sulfur (Fe–S) cluster known as F_B.[3–5] Photosystem (PS) is renowned for its high quantum efficiency, acting as an exceptional photoconverter by harnessing the photochemical properties of chlorophyll molecules in concert with electron-transfer proteins such as cytochrome enzymes.

---

[a] *Nano and Bioelectrochemistry Research Laboratory, CO_2 Research and Green Technologies Centre, Vellore Institute of Technology University, Vellore – 632 014, Tamil Nadu, India. E-mail: askumarchem@yahoo.com, askumar@vit.ac.in; Tel: +91-416-2202754*

[b] *Department of Chemistry, School of Advanced Sciences, Vellore Institute of Technology University, Vellore – 632 014, Tamil Nadu, India*

[c] *Department of Bioscience, School of Bio-Sciences and Technology, Vellore Institute of Technology, Vellore, Tamil Nadu 632014, India*

[d] *Department of Chemistry, SRM Institute of Science and Technology, Kattankulathur 603203, Tamil Nadu, India*

[e] *Department of Chemistry, Sri Ramakrishna Mission Vidyalaya College of Arts and Science, Coimbatore-641020, Tamil Nadu, India*

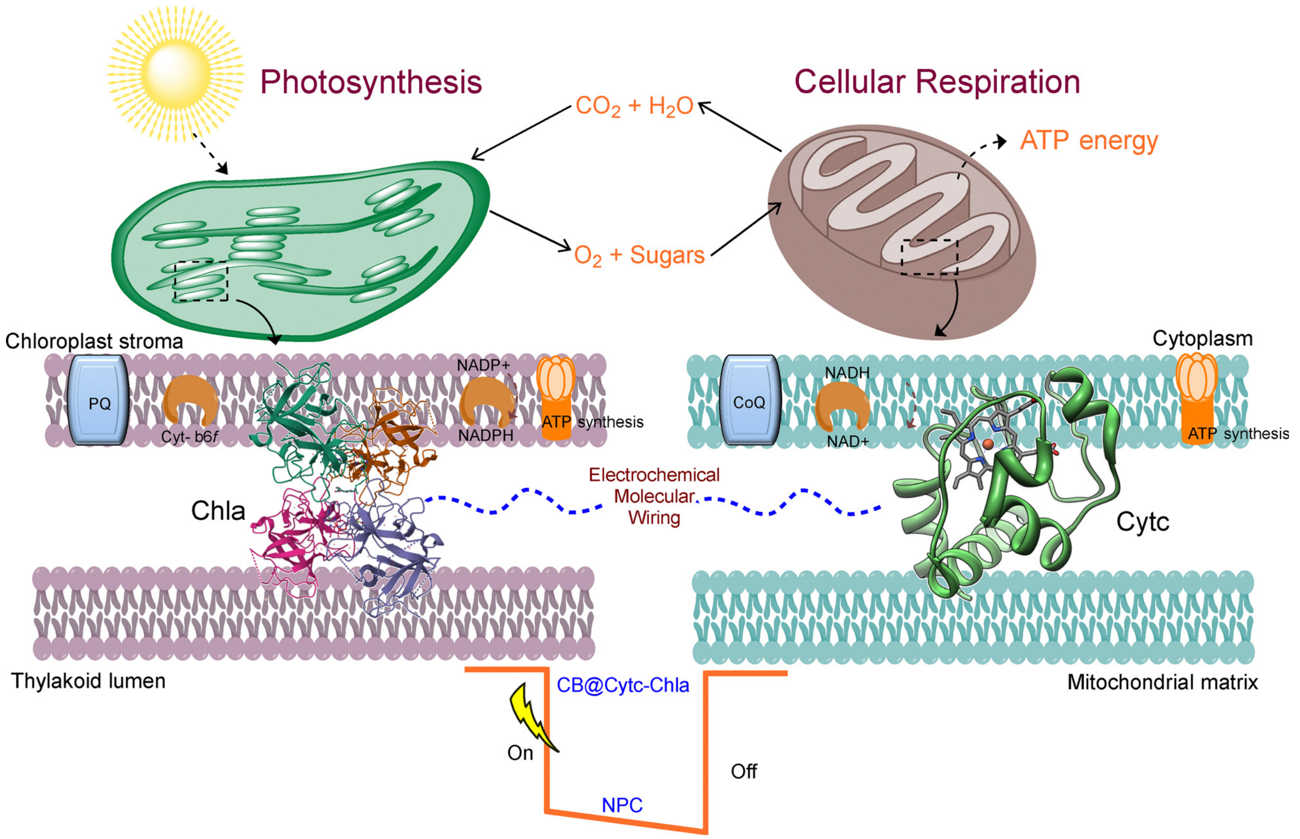

Scheme 1 A schematic illustration depicting the electrochemical molecular wiring involved in proton-coupled electron transport, occurring at the chloroplast during photosynthesis and within the cytoplasm during cellular respiration *via* several compartmental sessions. (Chl*a* – chlorophyll *a*; Cytc – cytochrome *c*; NPC – negative photocurrent; CB – carbon black).

Reconstructing such mechanisms in artificial systems presents exciting opportunities for applications in solar energy harvesting,[1,6–8] biosensing,[9,10] and biomedical technologies.[11] Cytochrome *c* (Cytc), although best known for its role in mitochondrial electron transport, also functions as a highly stable and reversible electron carrier.[12,13] In cyanobacteria, the analogous protein, cytochrome c_6, serves a similar role.[14] The presence of a heme prosthetic group allows Cyt*c* to shuttle electrons efficiently between redox partners.[15] Notably, in certain algae and cyanobacteria, c-type cytochromes have been shown to directly transfer electrons to Chl*a* within the thylakoid lumen of chloroplasts,[16] highlighting their potential in synthetic analogues of natural photosystems. Note that in plants, photosynthesis captures light energy within chloroplasts to convert carbon dioxide and water into glucose and molecular oxygen. Conversely, in mitochondria, eukaryotic cells oxidize glucose and other metabolites through the process of cellular respiration *via* a series of redox-active protein complex systems (Scheme 1).[4] While photosynthesis and respiration are traditionally viewed as compartmentalized and distinct processes (Scheme 1), recent advances in synthetic biology and nanobioelectronics have opened possibilities for interfacing these energy systems *via* artificial electron pathways. In particular, electrical molecular wiring strategies have emerged as promising approaches to directly connect redox components from photosynthetic and respiratory chains, enabling the design of hybrid systems that exploit light-driven energy capture to control or enhance biological oxidation–reduction reactions.[12,15]

In recent years, artificial photosystems have emerged as promising bioelectrochemical platforms that mimic the light-harvesting and electron-transfer functions of their biological counterparts.[17–19] A critical challenge in the design of these systems is achieving direct electron transfer (DET) between the photosynthetic pigment, such as Chl*a* and the underlying electrode surface,[20–22] which is essential for efficient electron flow and system performance. In this study, we report a simple fabrication of an artificial PS composed of Chl*a* and Cyt*c* immobilized onto carbon black (CB) nanomaterials using a simple chemical immobilization technique. This hybrid construct demonstrates efficient solar energy conversion and enables bio-electrocatalytic reduction of hydrogen peroxide, with further application in the detection of reactive oxygen species (ROS) in cancer cell systems. This work offers a pathway toward the development of multifunctional bioelectronic platforms with applications in renewable energy and biomedical diagnostics.

Electrical wiring of Chl*a* refers to the diverse chemical strategies employed to electronically connect the photoactive chlorophyll special pair (P700) within PS to an electrode or redox mediator.[20–23] This connection is critical for enabling efficient DET, a key step in bioelectronic and photoelectrochemical applications. However, achieving DET is particularly challenging due to the deeply embedded nature of the chlorophyll cofactors within PS's macromolecular protein structure, which is inherently dielectric and hinders efficient electronic coupling with external conductive surfaces. Simple physical adsorption of Chl*a* onto an electrode surface often results in an outer-sphere electron transfer process, where electrons must tunnel through the protein matrix to reach the active site.[24] This electron tunnelling is inherently inefficient, leading to poor electrochemical performance. To overcome these limitations, a wide range of chemical strategies – collectively referred to as molecular wiring – have been developed to establish more effective electronic communication between Chl*a* and electrodes. A central approach involves the use of functionalized electrode surfaces that can form stable linkages with Chl*a* through covalent bonding,[25] non-covalent interactions such as π–π stacking or electrostatic attraction,[20,21,26–29] or *via* self-assembled monolayers (SAMs).[22,30–33] These engineered interfaces promote inner-sphere electron transfer,[34] which greatly enhances the efficiency of DET by facilitating closer and more directed interactions between the electrode and the Chl*a* reaction centre. Over the years, several molecular species and strategies have been reported in the literature for wiring Chl*a*, particularly targeting the chlorophyll-containing regions. These include thiol-terminated SAMs on gold[30,33] or ITO electrodes,[35,36] aromatic linkers such as pyrene derivatives for π–π interactions, redox-active polymers that serve as mediators, and conductive nanomaterials like graphene oxide[20,21,26–29] and carbon nanotubes[37] that offer both structural support and electronic connectivity. Through these approaches, researchers aim to overcome the intrinsic limitations posed by Chl*a* complex architecture, enabling its integration into advanced bioelectronic devices and artificial photosynthetic systems. In a notable study conducted in 2001, Kievit and Brudvig demonstrated a non-covalent interaction-based approach for PS immobilization.[20] They reported the binding of plastocyanin (Pc), a PS-associated electron carrier, to cytochrome *c* in a surfactant-containing solution. This interaction was driven by hydrophobic forces and electrostatic attraction. The half-wave potential of Chl*a* in this configuration was observed to be $E_{1/2}$ = 490 mV *vs.* SHE, confirming the electrochemical activity of the immobilized PS. The underlying mechanism involves the positively charged lysine residues near the heme group of Cyt*c* interacting with the negatively charged region and hydrophobic patch on Pc, facilitating binding between the proteins. However, this approach resulted in a relatively weak peak current and poor electrochemical response, highlighting limitations in DET efficiency. Subsequent approaches involved the fabrication of chemically modified heterogeneous electrodes to promote more stable and efficient Chl*a* immobilization.[21,37] For instance, covalent attachment of PS *via* self-assembled monolayers on gold[22,30–33] and indium tin oxide (ITO) electrodes was achieved using mercaptoethanol-based linker molecules. Alternatively, non-covalent strategies utilized graphitic substrates to anchor PS through π–π interactions.[20,21,26–29] These configurations showed promising photocurrent responses under aqueous conditions, indicating functional photoelectrochemical activity. Despite their advantages, these methods often involve labour-intensive and time-consuming preparation steps. Notably, the formation of mercaptoethanolic SAMs on gold electrodes and subsequent PS immobilization can take up to seven days, limiting scalability and practical application.[22,30–33] To address these limitations, a more rapid and straightforward technique, vacuum-assisted drop-casting, has been employed. In this method, an aqueous suspension of PS is deposited onto a substrate, and negative pressure is applied to remove the solvent.[38] This results in the formation of a residual multilayer PS film. The assembly of these films is thermodynamically driven by hydrophobic interactions between neighbouring PS complexes, leading to stable film formation without the need for prolonged chemical modification steps. Interestingly, in this work, we develop a successive drop-casting of a diluted solution of Chl*a* and Cyt*c* solution on a carbon black nanomaterial modified underlying electrode, such as glassy carbon and disposable type screen-printed carbon electrode, which requires only 30 minutes of working time and shows excellent molecular wiring and DET reactions.

Graphitic carbon-based materials have emerged as promising substrates for constructing biocompatible applications, due to their large surface area, excellent electrical conductivity, and the presence of interconnectable carbon–oxygen functional groups that facilitate efficient electron transfer.[39–41] Among these, carbon black (CB) stands out as a cost-effective and versatile option. It is a fine, carbon-rich powder primarily composed of elemental carbon in the form of near-spherical particles and aggregates, typically produced through the incomplete combustion or thermal decomposition of hydrocarbons.[42] While it lacks the high degree of structural order seen in materials like graphene or carbon nanotubes, CB exhibits partially graphitic domains within an overall amorphous carbon matrix. Its surface is chemically diverse, containing a mixture of sp^2 and sp^3 hybridized carbon atoms and various functional groups such as hydroxyl, carboxyl, and carbonyl groups.[43,44] These functionalities enhance its reactivity and enable strong interactions with a wide range of molecules, including biomolecules like enzymes and proteins. The nanostructured morphology of carbon black, combined with its high conductivity, supports efficient electron transfer by minimizing electron tunnelling distances and reducing resistance. Additionally, its porous structure allows for the immobilization of multilayer enzyme assemblies, potentially increasing catalytic activity while ensuring adequate diffusion of substrates and products. These combined features make carbon black an attractive material for applications in bioelectrochemical systems, including biosensors, enzymatic fuel cells, and artificial photosynthetic devices[44, 43]. For the first time in the literature, CB has been utilized as a matrix for the molecular wiring of Chl*a* and Cyt*c* biomolecules. This hybrid system demonstrated highly efficient bio-electron transfer, enabling both effective photocurrent generation and bio-electrocatalytic reduction of H_2O_2 in phosphate buffer solution at pH 7. The resulting bioelectrode was thoroughly characterized using a range of physicochemical and electrochemical techniques, including *in situ* scanning electrochemical microscopy (SECM) and electrochemical quartz crystal microbalance (EQCM) analysis. Furthermore, the CB@Cyt*c*–Chl*a* assembly was employed as a sensitive peroxide detector using the batch injection analysis method. This approach was successfully applied to monitor reactive oxygen species (ROS) generated under induced stress conditions in tumor cells, demonstrating the potential of the system for biomedical sensing applications. Although there were few non-enzymatic sensors developed for this purpose,[45–47] which in general are expected to show unknown interference, this work demonstrated bioelectrodes for sensing purposes. Overall, this study focuses on elucidating the molecular wiring and electron-transfer interactions between Chl*a* and Cyt*c* immobilized on a heterogeneously modified carbon electrode. Notably, the electrochemical coupling between Chl*a*, the photosystem I pigment, and Cyt*c* has not been previously reported. The co-immobilization of these biomolecules on carbon nanomaterials led to a markedly enhanced electron-transfer process, as evidenced by a reduced overpotential and increased current during the bioelectrocatalytic reduction of hydrogen peroxide, confirming the efficiency of the molecular wiring strategy.

2. Experimental section

2.1. Materials

Cytochrome *c* protein from the bovine heart (12 230 Da) and bovine serum albumin (98% purity) were obtained from Sigma Aldrich®. Plant-derived chlorophyll a (C0780-TCI chemicals, Japan; ~98% purity) plant-derived chlorophyll was utilized as the primary photoactive molecule, functionally representing the active site of Photosystem I. Carbon black (CB, N330 grade gifted from Phillips Carbon Black Ltd, Kochi, India) and H_2O_2 (30%; Rankem) were used as received and stored. A pH 7 buffer (0.1 M ionic strength) was prepared by mixing appropriate concentrations of Na_2HPO_4 and NaH_2PO_4 and was used as a supporting electrolyte under N_2 purged conditions. Caution! Since H_2O_2 exposure can cause a stinging sensation on the hands, the chemical should be handled using appropriate safety protection. Chlorophyll is highly light sensitive, handled in dark conditions, and a N_2 atmosphere and all the experiments should be carried out in a dark room. MDA-MB-231 triple-negative breast cancer cells were provided by Tamizhselvi Ramasamy (VIT-Vellore).

2.2. Apparatus

We conducted cyclic voltammetry experiments using a CHI 440B Electrochemical Workstation (USA). The setup included a three-electrode system: a glassy carbon electrode (GCE; 3 mm diameter) as the working electrode, Ag/AgCl (3 M KCl) as the reference electrode, and platinum (2 mm diameter) as the counter electrode. The cell had a 10 mL volume and was purged with N_2 gas. For scanning electrochemical microscopy (SECM), we used a Princeton Applied Research (PAR, USA) Versa scan-bi-potentiostat device in redox-competition mode (RC-SECM). The SECM setup included a GCE with a geometric area of 0.0707 cm^2 and a 10-μm Pt_{Tip} ultra microelectrode (UME) under bi-potentiostat conditions. Before the experiment, we fixed the position of the Pt_{Tip} relative to the SECM-Au substrate using an approach curve in feedback mode. This curve was obtained by moving the Pt_{Tip} position at speeds ranging from 1 to 100 $\mu m\ s^{-1}$ along the *z*-axis while maintaining a fixed applied potential of −0.4 V *vs.* Ag/AgCl. The screen-printed carbon electrode (SPE; 2 mm diameter) system customized for batch injection analysis (BIA) was purchased from Metrohm, Netherlands. An electronic-robot pipette was procured from Glisom. Raman spectroscopic analysis was conducted with a 532 nm laser excitation, Alpha300/WITec. AFM studies were performed using the Park NX20 AFM instrument system from South Korea. FT-IR spectroscopy was performed with a JASCO FT-IR-460 PLUS FRP, Japan. Zensor R&D Wireless-Potentiostat ECWP100 Single was used for a cancer cell study. Zensor R&D (Taiwan) disposable carbon screen-printed electrodes (SPE, 2 mm diameter) served as the base for FESEM, AFM, and Raman characterizations. CV-EQCM analysis used a gold single-crystal electrode (EQCM-Au, geometric surface area, 0.196 cm^2). The current–voltage (*I*–*V*) characteristics and the photoconductivity of the CB@Cyt*c*–Chl*a* were studied using a CEL-S500 Simulated Sunlight Xenon Light Source.

2.3. Preparation of GCE/CB@Cyt*c*–Chl*a*

Prior to the analysis, the GCE surface was mechanically cleaned using the BAS polishing kit and 0.05 μm alumina powder and washed with double-distilled water twice to flush out any loosely attached material on the surface. The sample was then cleaned using double-distilled water. Using potential cycling with 20 segments and a voltage window of −0.7 to 0.7 V *vs.* Ag/AgCl at a scan rate (ν) of 50 $mV\ s^{-1}$ in a pH 7 phosphate buffer (PB) solution, the cleaned electrode surface underwent electrochemical pretreatment. CV experiments were performed in a nitrogen-saturated solution medium. The GCE/CB@Cyt*c*–Chl*a* electrode was prepared by drop-casting of 3 μL of CB ethanol dispersion that had been prepared (2 mg in 500 μL of ethanol) and a 3 μL drop of cytochrome *c* oxidase dispersion (5 mg/500 μL of PBS), and allowed to dry for 20 minutes at room temperature. The modified electrode surface was dipped into Chl*a* (30 mg) dissolved in 10 mL of N_2-purged pH 7 PB solution (Scheme 2). Electrochemical characterization was subsequently performed using the modified electrode.

2.4. Photocurrent analysis

The photocurrent experiments were performed using a solar simulator involving a special photochemical system. This system consists of a CEL-S500 simulated sunlight xenon light source (Beijing, China) and a specialized separator. During all photocurrent measurements, the 10 mL electrochemical cell was used. Bioelectrodes were modified on a carbon screen printed electrode (SPE/CB@Cyt*c*–Chl*a*) similar to the method mentioned in the above session and placed having a fixed distance of 100 mm between each other with a beam diameter of 50 mm. The chronoamperometry (CA) technique was used to

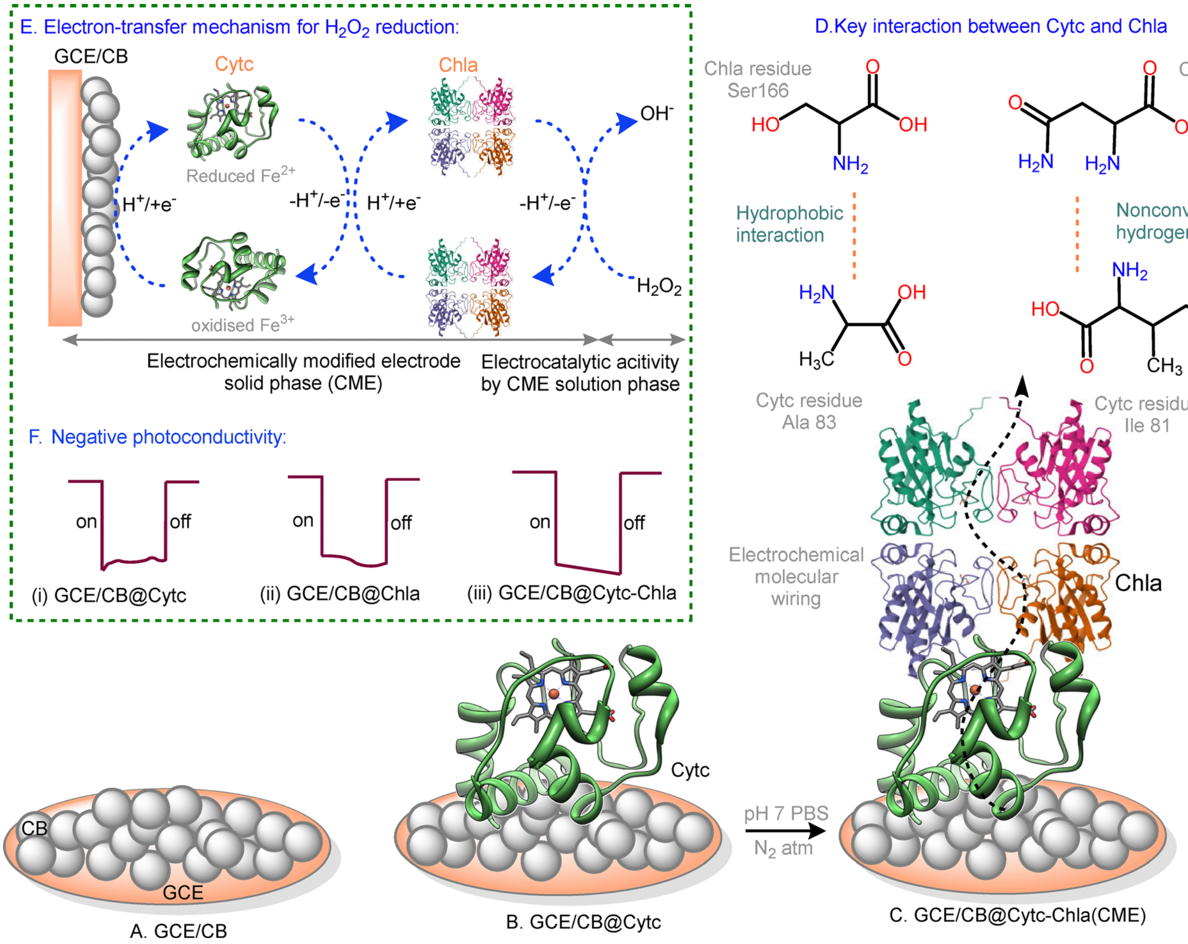

Scheme 2 (A)–(C) Schematic representation of the stepwise electrochemical assembly of cytochrome *c* (Cytc) and chlorophyll *a* (Chl*a*) onto a carbon black (CB)-modified glassy carbon electrode (GCE) in phosphate-buffered saline (PBS, pH 7) under a nitrogen atmosphere and dark conditions. (D) Illustration of the key non-covalent interactions facilitating complex formation between Cytc and Chl*a*. (E) Electrochemical activity of the CB-modified GCE following sequential modification with Cytc and Chl*a*, demonstrating mediated reduction of hydrogen peroxide (H_2O_2). (F) Observation of negative photoconductivity responses from CB@Cytc, CB@Chl*a*, and the CB@Cytc–Chl*a* hybrid interfaces.

perform photo-bioelectrochemical experiments, and 0.1 M pH 7.4 PB solution was used as an electrolyte. All CA measurements were performed by using a potentiostat upon cyclic on–off illumination at a light intensity of 50 W m^{-2} measured at the electrode surface.

2.5. Computational methodology-molecular docking study of Cytc and Chl*a* interaction

The crystal structures for Chl*a* (2DRE)[48] and cytochrome *c* (1HRC)[49] were downloaded from the protein data bank (PDB). Chl*a* has four chains (A, B, C, and D) with 180 amino acids, whereas cytochrome *c* has 105 amino acids. The pyDockWEB[50] was employed for molecular docking, an efficient tool for predicting rigid-body protein–protein interactions. It predicts 10 000 conformations using the FTDock sampling method, which utilizes the FFTW library to scan translational and rotational freedom. Finally, 10 000 different conformations were obtained relying on the scoring functions. VMD[51] and pyMOL[52] were used for the visualization of the docking conformations.

3. Result and discussion

3.1. Electrochemical biomolecular wiring of Cytc and Chl*a* on the CB surface

Fig. 1A presents the comparative CV responses of GCE/CB@Cytc, GCE/CB@Chl*a*, and GCE/CB@Cytc–Chl*a* electrodes recorded under dark conditions in nitrogen-purged phosphate buffer solution (pH 7). For GCE/CB@Cytc and GCE/CB@Chl*a*, a predominant cathodic current was observed at approximately potential, −0.35 V *vs.* Ag/AgCl, which can be attributed to the irreversible reduction of redox-active sites within the protein units. This suggests a lack of effective electronic communication between the individual protein layers and the underlying carbon electrode, indicating poor molecular linkage. In contrast, the GCE/CB@Cytc–Chl*a* electrode exhibited a well-defined quasi-reversible redox couple centered at an apparent formal potential ($E^{\circ\prime}$) of −0.15 V *vs.* Ag/AgCl, which is ∼0.2 V more positive than the signals observed for the individual protein-modified electrodes. Additionally, a minor irreversible peak appeared around 0.1 V *vs.* Ag/AgCl. This shift in redox

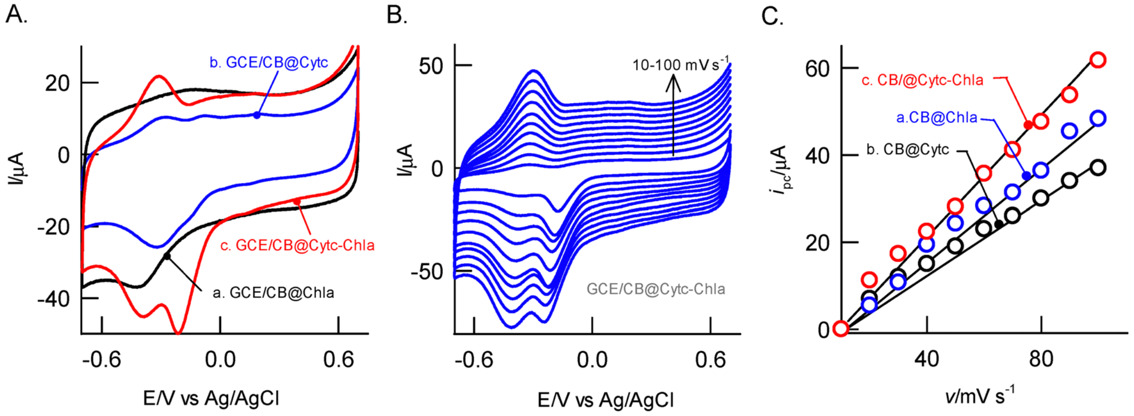

Fig. 1 CV responses of (A) different modified electrodes: (a) GCE/CB@Chl*a*, (b) GCE/CB@Cyt*c*, and (c) GCE/CB@Cyt*c*–Chl*a* in blank pH 7 PBS solution (N_2 purged) under dark conditions. Scan rate: 50 mV s^{-1}. (B) The effect of the scan rate (10–100 mV s^{-1}) of GCE/CB@Cyt*c*–Chl*a* in blank pH 7 PB solution and (C) the respective plots of modulus i_{pc} (modulus) *vs.* *v*.

potential, along with improved signal definition, suggests the formation of an efficient molecular wiring network between Cyt*c* and Chl*a* units immobilized on the CB surface, enabling facilitated electron transfer.

The molecularly wired configuration (Chl*a*–Cyt*c*) exhibits enhanced redox features compared to the individual components, indicating improved electron transfer efficiency at the electrode interface. The surface coverage (Γ) of the GCE/CB@Cyt*c*–Chl*a* electrode was calculated to be 2.96×10^{-9} mol cm^{-2}. Furthermore, twenty successive CV scans at a scan rate of 50 mV s^{-1} showed a relative standard deviation of 3.4% for the cathodic peak current (i_{pc}), indicating excellent electrochemical stability of the modified electrode. The optimal loading concentration of Chl*a* was determined to be 5 μL of a 10 mg mL^{-1} solution, which likely provides the maximum molecular interaction between Cyt*c* and Chl*a* under the given conditions (see SI, Fig. S1).

As a control experiment, a porphyrin ligand lacking a central metal ion (Mg^{2+}; similar to natural chlorophyll) was immobilized on the electrode surface and evaluated for its redox behavior. Fig. S2(A and B) present the CV responses of GCE/CB@Porphyrin and GCE/CB@Cyt*c*-Porphyrin in a pH 7 phosphate buffer solution. The CB@Porphyrin-modified electrode showed no discernible redox peaks, indicating an absence of electron-transfer activity. Similarly, the CB@Cyt*c*-Porphyrin-modified electrode displayed a markedly reduced current response – approximately fourfold lower than that of the active Chl*a*-based system. These observations underscore the essential role of the central Mg^{2+} ion in the Chl*a*, which facilitates effective molecular wiring and promotes efficient electron transfer between the porphyrin ring and the cytochrome *c* protein anchored on the carbon black surface. Based on the observations, the prominent redox peak identified in this study is attributed to Chl*a* with Mg^{2+}/Mg^{+} redox sites, which are electrochemically activated through the redox process of Cyt*c*–Fe^{3+}/Fe^{2+}. The minor irreversible peak observed in the CV of Fig. 1A, curve c, is attributed to the electron-transfer behavior of the Cyt*c*–Chl*a* system immobilized on energetically heterogeneous active sites of carbon black, particularly at locations associated with trace-level metal impurities.

To understand the electron-transfer reaction, the CB@Cyt*c*–Chl*a* was subjected to the effect of scan rate experiments. Fig. 1B shows the gradual increase in the peak current values (modulus) while the scan rate increases from 10 to 100 mV s^{-1}. The plot of the cathodic peak (i_{pc}) current signal scan rate is linear in both cases, starting from the origin, indicating the surface-confined electron transfer of the CB@Cyt*c*–Chl*a* (Fig. 1C), which is a comparatively good response compared with CB@Chl*a* and CB@Cyt*c* (Fig. S3(A and B)). At the same time, the potential of CB@Cyt*c*–Chl*a* shows a gradual shift with increasing scan rate, as shown in Fig. S3C. This may be attributed to the large dielectric part of the protein on the underlying surface and the electron transfer of molecular wiring between the two biocomponents when the Cyt*c* interacts with Chl*a*.[13,53] Similarly, our previous study with the folded and unfolded Chl*a* on naphthoquinone shows the double-time decrement in current value due to the same effect of large dielectric and intrinsic resistance.[15,53] Overall, the CB@Cyt*c*–Chl*a* exhibited a unique, redox-active molecular electrode with enhanced molecular wiring.

3.2. Physicochemical characterization of the modified electrode

Fig. 2 depicts the comparative imaging of FESEM (A–C), 2D-Raman (D–F), and AFM (G–I) images of the CB, CB@Chl*a*, and CB@Cyt*c*–Chl*a*. In FESEM, Fig. 2A and B of CB and CB@Chl*a* showed agglomerated structures with flabby and cloudy morphologies. Whereas, CB@Cyt*c*–Chl*a* (Fig. 2C) represents the flake-like composite material surface, which is due to the coverage of Cyt*c*–Chl*a* composite on the electrode surface. The 2D Raman imaging (Fig. 2D–F) provides critical insights into materials' spatial distribution and interactions across three modified electrodes: SPE/CB, SPE/CB@Chl*a*, and SPE/CB@Cyt*c*–Chl*a*. The images highlight the distribution of materials (represented by colour contrast regions) and their interactions. In Fig. 2D, the distribution of red and blue regions shows a uniform coverage of agglomerated CB over the SPE surface. This uniformity is crucial for enhancing electrode conductivity

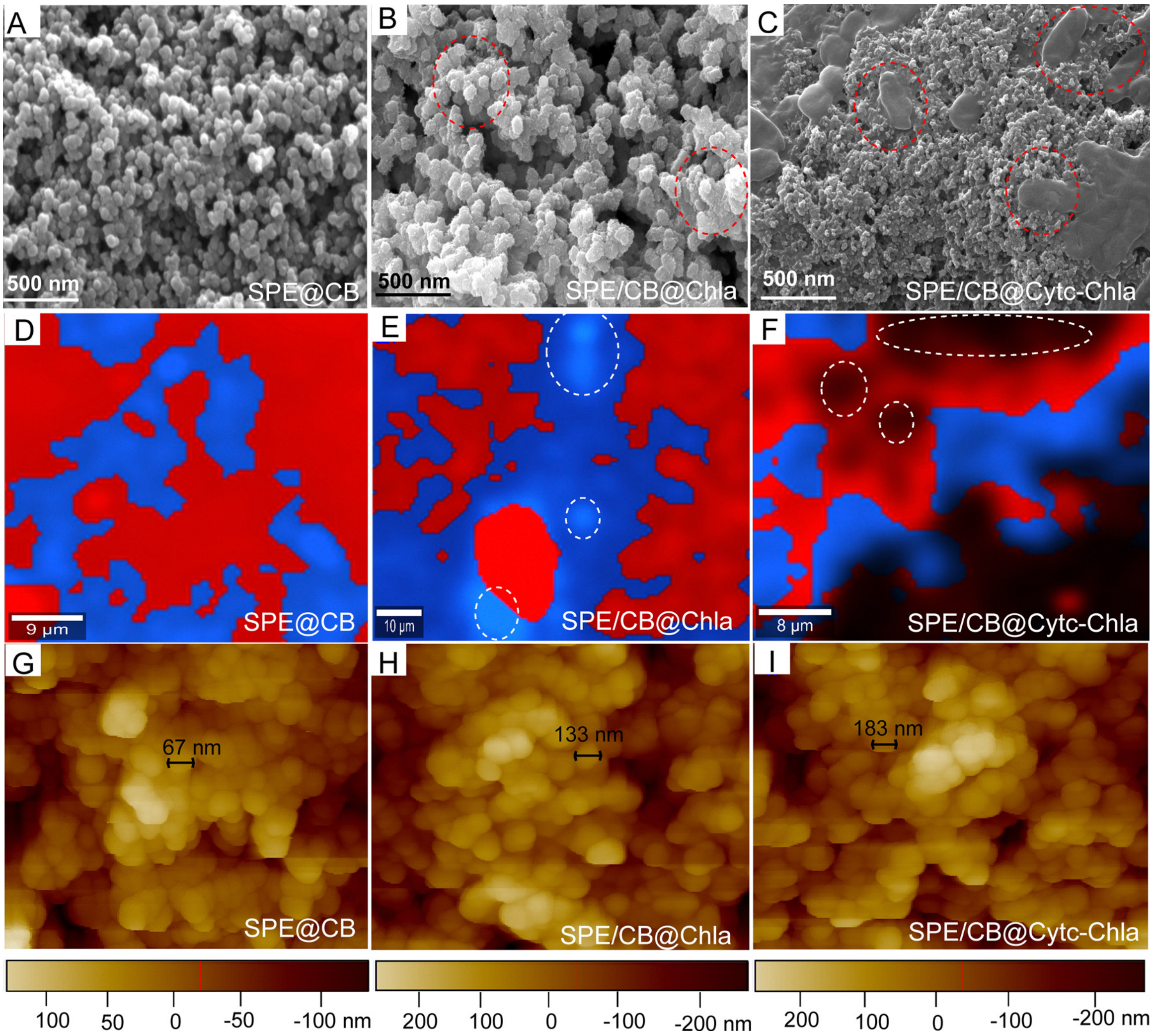

Fig. 2 FESEM (A)–(C), 2d-Raman mapping (D)–(F), and AFM (G)–(I) images of CB, CB@Chl*a* and CB@Cytc–Chl*a*.

and surface area. Whereas in Fig. 2E, CB@Chl*a*, the white ovals highlight areas where Chl*a* aggregates or interacts with CB, suggesting strong material integration. Overlapping red and blue regions indicate interfacial interactions between CB and Chl*a*, which are essential for enhancing charge transfer processes. Furthermore, in CB@Cyt*c*–Chl*a* (Fig. 2F), the addition of Cyt*c* creates a complex and denser distribution pattern, with the blue regions becoming more pronounced. The white ovals emphasize key interaction zones, where Cyt*c* effectively integrates with the CB and Chl*a* layers. Enhanced overlap between red and blue regions suggests robust interfacial interactions among CB, Chl*a*, and Cyt*c*. This synergistic interaction likely improves the electrode's bio-electrochemical activity. As shown in Fig. 2(G–I), AFM was used to analyze the surface distribution of CB, CB@Chl*a*, and CB@Cyt*c*–Chl*a* as it represents the adsorbed matrix on the electrode. Spherical highly agglomerated micro-ball-like structures were noted as arrangements for all three cases, and based on the contour profiles, each modification of CB, Chl*a*, and Cyt*c* was calculated (Fig. S4). The diameter of each system was changed and gradually increased on step-by-step modifications, namely, CB shows 65 ± 7 nm, CB@Chl*a* shows 130 ± 9 nm and the CB@Cyt*c*–Chl*a* shows 180 ± 11nm. The diameter of each system increased by double the amount for each modification. This may be attributed to the structural arrangements and orientation of good molecular interactions between the Chl*a* and cytochrome *c* for proper ET transfer.

Fig. 3A(a–e) represents the FTIR response of CB, CB@Chl*a*, Cyt*c*, CB@Cyt*c*, and CB@Cyt*c*–Chl*a*, which were analyzed to validate the chemical functional groups responsible for the stabilization of Chl*a* and Cyt*c* molecular interactions. The CB network system showed poor IR signals (Fig. 3A, curve a). For the case of CB@Chl*a*, marked IR signals corresponding to the –OH or –NH peak (3220 cm^{-1}) CH═CH (aromatic, 2918 cm^{-1}) O═C═O (2340 cm^{-1}), C═O (1642 cm^{-1}) and metal nitride (M–N) (630 cm^{-1}) which represents the pyrrole ring, hydrocarbon, and phytol tail and metal nitride functional groups were noticed which confirms the immobilization of Chl*a* on CB (Fig. 3A, curve b). Similarly, for the case of the control Cyt*c*-protein, IR peaks due to the overlapped signals of –OH/–NH

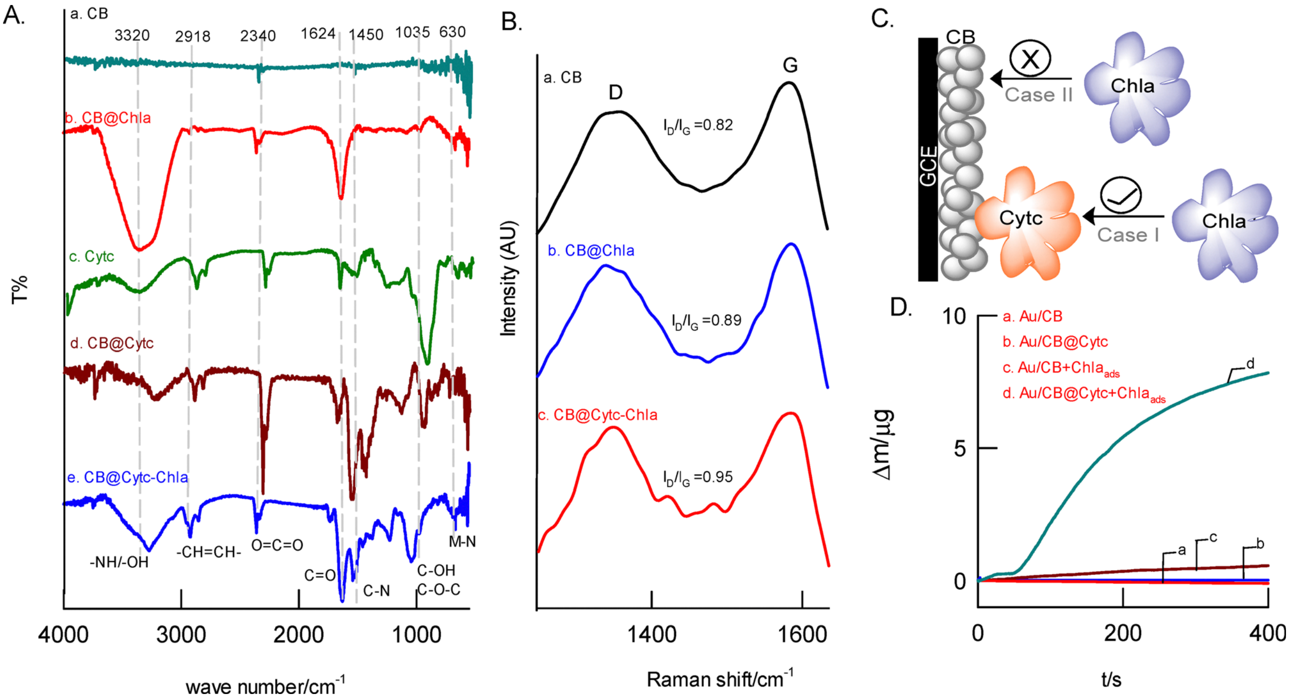

Fig. 3 (A) FT-IR response of (a) CB, (b) CB@Chl*a*, (c) Cyt*c*, (d) CB@Cyt*c*, and (e) CB@Cyt*c*–Chl*a* and (B) Laser Raman response of (a) CB, (b) CB@Chl*a* and (c) CB@Cyt*c*–Chl*a*. (C) illustration of the absorption of Chl*a* on Cyt*c* and (D) EQCM response of various modified electrodes in the time *vs.* frequency mode: (a) Au/CB, (b) Au/CB@Cyt*c* (c)Au/CB + Chl*a* and (d) Au/CB@Cyt*c* + Chl*a* in pH 7 PBS (N_2 purged).

(3320 cm^{-1}), metal nitride peak (630 cm^{-1}) and –CH=CH– (aromatic, 2918 cm^{-1}) and specific signals for the amide I (1624 cm^{-1}) and C–OH/C–O–C (1035 cm^{-1}) were noticed (Fig. 3A, curve c). When the above systems were combined, unique IR responses were observed. According to a report, due to tryptophan pockets opening and contact with hydrophobic aromatic sites, the amide began to break, and the aromatic –CH=CH– functional groups were denser following protein unfolding. Following Cyt*c*'s immobilization on the CB surface, there was a noticeable noisy response and a considerable drop in amide signal strength (Fig. 3A, curve d). Interestingly, when the optimal system, *i.e.*, CB@Cyt*c*–Chl*a* was subjected to IR, obvious retainment of the characteristic IR signals of Chl*a* and Cyt*c* fingerprints especially amide (3320 cm^{-1}) and –CH=CH– (2918 cm^{-1}) and the metal nitride peak (630 cm^{-1}) which represents the successful encapsulation of Cyt*c*@Chl*a* on the porous structure of CB (Fig. 3A, curve e).[53,54] The graphitic structure of CB/Chl*a* (i) and Cyt*c*/Chl*a* protein (ii) exhibits a solid connection through π–π bonding, as demonstrated by these studies, and the amide bands on the CB@Cyt*c*–Chl*a* are retained without any denaturalization (folded nature).

To further confirmation of molecular interaction, the samples, CB, CB@Chl*a*, and CB@Cyt*c*–Chl*a* modified electrode, were examined by laser Raman spectroscopic analysis. All samples exhibit qualitatively identical D and G bands in Fig. 3B, curves a–c, corresponding to the disordered sp^3 and ordered sp^2 carbons, respectively, at roughly 1300 and 1500 cm^{-1}. After calculating the intensity ratio (I_D/I_G) between the D band and G bands, it was discovered that the modified electrode with CB (0.82) had a much lower value than the values observed with CB/Chl*a* (0.89) and CB@Cyt*c*–Chl*a* (0.95). This observation links the surface alteration to a particular increase in the G band. The possible causes include (i) the increase in sp^2 carbon units brought on by CB, (ii) layer-by-layer stacking on the graphitic structures on the surface of CB underneath, and (iii) a surface that has more graphitic heteroatoms.[55,56]

To further investigate the highly specific interaction between Cyt*c* and Chl*a*, an *in situ* EQCM experiment was conducted, as shown in Fig. 3C and D. EQCM is a reliable and sensitive technique that enables real-time monitoring of changes in surface mass during electrochemical processes. In this study, we explored the potential for specific Cyt*c*–Chl*a* interactions by modifying the EQCM electrode surface with one protein (Cyt*c*) and exposing it to a solution containing the other (Chl*a*). If specific binding occurs between the two proteins, a measurable increase in the mass of the quartz crystal is expected due to the added mass, as shown in Fig. 3D. To test this, an EQCM crystal modified with a CB@Cyt*c* composite (EQCM-Au/CB@Cyt*c*) was used as the working electrode, and a dilute Chl*a* solution in pH 7 phosphate buffer (PB) was used as the electrolyte solution. Change in mass *versus* time measurements were carried out for 400 seconds under nitrogen-purged conditions. Initially, control experiments were performed using bare EQCM-Au/CB, EQCM-Au/CB + Chl*a*, and EQCM-Au/CB@Cyt*c* in PB solution (pH 7). Both EQCM-Au/CB and EQCM-Au/CB@Cyt*c* showed minimal changes in mass, indicating stable surface configurations in the absence of any marked mass change on the surface. Subsequently, EQCM-Au/CB was

Table 1 The docking conformations and their energies in kcal mol^{-1}

Docking conformations	Electrostatics	VDW	Desolvation	Total docking score
Dock1	−45.9	24.9	5.4	−37.9
Dock2	−50.7	5.1	14.2	−36.0
Dock3	−49.8	78.9	6.4	−35.5

exposed to Chl*a* solution (EQCM-Au/CB + Chl*a*), which also resulted in negligible mass changes, suggesting no specific interaction between Chl*a* and CB. These results provide strong evidence for the specific binding between Cyt*c* and Chl*a*, mediated by the CB-modified electrode surface.

The enzyme immobilization process was quantitatively monitored using the EQCM (Fig. 3D). The observed frequency shifts (Δf) were converted into corresponding areal mass changes (Δm) based on the Sauerbrey relationship:

$$\Delta m = \frac{\Delta f \times C}{n}$$

where constant (C) = −1.34 ng cm^{-2} Hz^{-1} for a 5 MHz AT-cut quartz crystal, and n = 1 represents the overtone number. The obtained areal mass was multiplied by the geometric electrode area (0.196 cm^2 for a 5 mm diameter electrode) to determine the total adsorbed enzyme mass. This mass was subsequently converted into enzyme surface loading (pmol cm^{-2}) using the molecular weights of cytochrome *c* (12.4 kDa) and chlorophyll *a* (0.893 kDa). For the Au/CB@Cyt*c* + Chla_{ads} electrode, a frequency decrease of approximately −6000 Hz corresponded to a mass uptake of $\sim 1.57 \times 10^{-6}$ g cm^{-2}, translating to an enzyme loading of ∼127 pmol cm^{-2}. The higher mass accumulation compared to individually modified electrodes suggests a synergistic co-adsorption of Cyt*c* and Chl*a*, resulting in a more compact and stable biofilm architecture. This cooperative immobilization likely enhances interfacial electron communication and contributes to the improved photoelectrochemical performance observed at the bioelectrode.

3.3. Molecular docking studies of Cyt*c*/Chl*a*

The top 3 docking conformations were selected for screening the docking score, and the docking structures are shown in Fig. S5. To obtain more insights into the interactions of docking conformations, the energy terms are tabulated in Table 1. Furthermore, the key interactions between the two proteins were studied. The Chl*a* residues of Asp162, Asp163, Ser166, Glu168 and Asn169 closely interact with cytochrome *c* (Thr28, Lys79, Ile81, and Ala83). Ser166 and Asn169 residues of Chl*a* show hydrophobic interactions with Ala83, Ile81, and Thr28 of cytochrome *c*. Moreover, Asp163 and Glu168 make nonconventional hydrogen bonding interactions with cytochrome *c*. The close interactions between two Chl*a* and cytochrome *c* are shown in Fig. 4. Furthermore, the nonconventional H-bonding and hydrophobic interactions with distances are shown in Table 2. This shows that these proteins have better binding modes and interactions.

3.4. *In situ* SECM imaging of the bio-electrocatalytic site of CB@Cyt*c*–Chl*a* in feedback mode

The central objective of this study is to image and evaluate the bioelectroactive sites on the electrode surface using SECM. To achieve this, we optimized the redox mediator system as $Fe(CN)_6^{3-/4-}$, which provides stable and well-defined electrochemical behavior without interference from side reactions. This redox couple exhibits reversible kinetics and does not participate in undesired homogeneous reactions with dissolved oxygen or hydrogen peroxide, thereby ensuring accurate mapping of surface electroactivity. In contrast, the methyl viologen (MV^{2+}/MV^{+}) redox couple ($E^\circ \approx -0.6$ V *vs.* Ag/AgCl at pH 7) often undergoes mediated redox processes involving dissolved oxygen and hydrogen peroxide under aqueous conditions, leading to the formation of reactive intermediates. Such interference complicates the interpretation of SECM feedback signals and can obscure the true electrochemical activity of the surface.

To visualize the electroactive and ET sites of the biomimicking system, we used different SECM operating conditions in this work, such as the feedback mode, where the $Fe(CN)_6^{3-/4-}$ redox couple is reduced and oxidized the substrate and tip of the SECM probe respectively,[53] and the feedback current obtained on the Pt-Tip was used to image the surface. SECM offers real-time applications for visualizing electroactive spots on the surface, in contrast to electron microscopic pictures, which provide the bulk morphology of the surface. Fig. 5A and B are typical SECM working mechanisms in the feedback mode that are employed to photograph the modified electrode surface of GCE/CB@Chl*a* and GCE/CB@Cyt*c*–Chl*a*. The substrate's potential was tuned to the reduction of $Fe(CN)_6^{3-}$ ($E_{\text{Sub}} = -0.25$ V) in this setup, and the Pt_{Tip} was used to re-oxidize it at 0.4 V *versus*

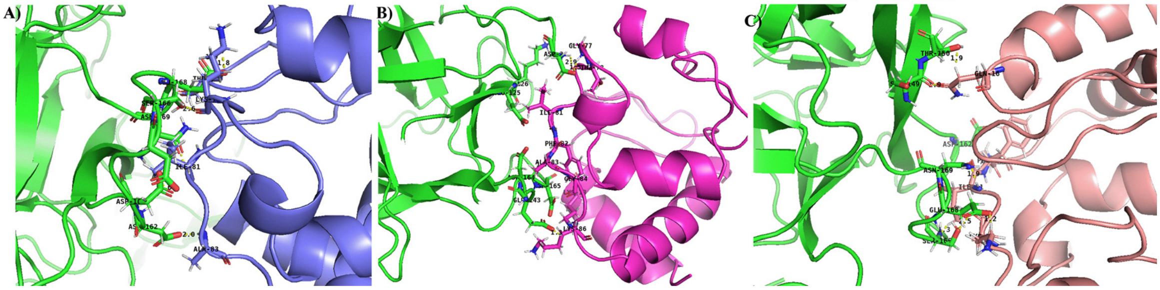

Fig. 4 The key interactions between Chl*a* and cytochrome *c*. (A) dock1, (B) dock2 and (C) dock3.

Table 2 The key interactions between Chl*a* and cytochrome *c* for the top 3 docking conformations

Docking conformations	H-bonding interactions (Å)	Hydrophobic interactions (Å)
Dock1	Asp162 HO···HC Ala83 (2.5) Asp163 O^-···HC Ile81 (1.7) Asp163 ═O···HC Ile81 (1.6) Asp163 ═O···HC Ile81 (2.1) Glu168 C═O···HC Lys79 (1.9) Glu168 O···HC Lys79 (1.8) Glu168 C═O···HC Thr28 (2.2)	Ser166 HO···O═C Lys79 (2.6) Ser166 NH···HC Ile81 (1.4) Asn 169 NH···HC Thr28 (1.8) Asn 169 C═O···O═C Ile81 (2.1)
Dock2	Glu143 C═O···HC Lys86 (1.9) Glu143 O^-···HC Lys86 (1.3) Asp164 C═O···HN Ala83 (1.7) Asp165 C═O···HC Phe82 (1.8) Glu125 C═O···HC Ile81 (1.5) Lys126 NH···CH Ile81 (1.8) Asp3 O^-···HN Gly77 (1.5) Asp165 O^-···HC Lys13 (1.6)	Asp165 C═O···O═C Gly84 (2.5) Asp164 CH···HC Ala83 (0.8) Glu125 CH···HC Ile81 (0.9) Asp3 NH···NH Thr78 (2.3) Asp3 NH···HC Gly77 (1.4)
Dock3	Asp162 O^-···HC Phe82 (2.0) Glu168 O^-···HC Lys79 (1.2) Asn169 C═O···HN Ile81 (1.9) Thr150 HO···HC Gln16 (2.5) Ser166 HN···HC Ile81 (1.3)	Asp162 CH···HN Ala83 (1.2) Asp162 CH···HC Ala83 (1.3) Ser166 NH···HC Ile81 (0.8) Ser149 C═O···O═C Gln16 (1.9) Thr150 CH···HC Gln16 (1.8) Ser166 HO···O═C Lys79 (2.5)

Ag/AgCl. Before the mapping examinations, the CV experiment of GCE/CB@Chl*a* and GCE/CB@Cyt*c*–Chl*a* with 5 mM $\mathrm{Fe(CN)_6}^{3-}$ at ν = 50 mV s^{-1} was performed (Fig. S6A). Notably, the GCE/CB@Cytc–Chl*a* electrode exhibited a twofold higher current response than GCE/CB@Chla in cyclic voltammetry.

The immobilized Chl*a* and cytochrome *c* molecular interaction enhances the electrical conductivity to the matrix, serving as a tool for pointing the CB@Cyt*c*–Chl*a* or GCE/CB@Chl*a* spots, which means that both with and without cytochrome *c* were analyzed for accurate spots. Before the experiment, the $\mathrm{Pt_{Tip}}$ was positioned as optimally as possible by moving it in the *z*-axis direction. Fig. S6(B and C) displays the corresponding approach curves of all the working electrodes of CB@Chl*a* and CB@Cyt*c*–Chl*a*. Conversely, comparison feedback mode SECM images of CB@Chl*a* and CB@Cyt*c*–Chl*a* are shown in Fig. 5C and D. Regarding CB@Cyt*c*–Chl*a* (Fig. 5D), four distinct current regions/spots (1–4) were detected, and the CB@Chl*a* (Fig. 5C) system shows the sprinkled coral-like structure of bright yellow, blue, and red spots with an average size of 5 ± 2 μm on the surface due to the feeble electrical conduction of the CB between Chl*a*. Whereas, CB@Cyt*c*–Chl*a* displays island/flying cloud spots with an average size window of 10–50 μm: spot-1, approximately 8 nA; spot-2, approximately 6 nA; spot-3, approximately 4 nA; and spot-4, approximately 2 nA. FESEM, AFM, and CV responses together with the $\mathrm{Fe(CN)_6}^{3-/4-}$ redox system reveal that spots 1 and 2 correspond to cytochrome *c* embedded sites, whereas spots 3 and 4 relate to Chl*a* and CB bulk sites, respectively. This represents that the CB@Cyt*c*–Chl*a* modified system has more electroactivity when compared to CB@Chl*a*.[57]

3.5. Photocurrent of CB@Cyt*c*–Chl*a*

To probe the photochemical reaction of the artificial photosynthesis, the current–voltage (*I–V*) was recorded using a CEL-S500 simulated sunlight xenon light source. For this purpose, CB@Cyt*c*–Chl*a* modified on a screen-printed carbon electrode was used as a working system. Xenon lights were chosen to replicate sunlight because they closely resemble natural sunlight, since Chl*a* is sunlight-sensitive. The bioinspired Cyt*c*–Chl*a* modified electrode exhibits a rather unique photo-response, opening up new possibilities for bio-photonic device applications. At a bias voltage of −0.25 V, the transient photoconductivity of modified electrodes with optically chopped pulses of width 350 sec has been assessed. This on/off cycle is carried out twice to ensure consistent measurements. The transient current response of different modified electrodes under light irradiation at different atmospheres is depicted in Fig. 6A and B, curves (a–c).

The photocurrent response was recorded under both nitrogen and air atmospheres to evaluate the effect of oxygen on the photoelectrochemical performance (Fig. 6A–C). CB@Cyt*c*–Chl*a* showed a significantly enhanced photocurrent in air compared to nitrogen, suggesting that oxygen serves as an effective terminal electron acceptor, as shown in Fig. 6C. Interestingly, O_2 purged electrolyte solution, showing about thrice increment in the photocurrent (PC) activity of the protein modified electrode systems, revealing the effective molecular quenching assisted photocurrent activity. This supports the hypothesis that Cyt*c* may aid in facilitating oxygen reduction at the modified electrode, further enhancing overall current output. The photoresponse was recorded for different immobilizations such as CB@Cyt*c*, CB@Cyt*c* and CB@Cyt*c*–Chl*a*. All modified electrodes show a sustained NPC response with different current ranges. Additionally, it is noted that every stage of immobilization has major effects on the conductivity and photosensing on/off ratio. The following formula (1) has been used to compute the photoconductance yield (*Y*), which is the change in current due to radiation with respect to dark current.[58,59]

$$Y\ (\%) = \frac{I_{\mathrm{p}} - I_{\mathrm{dark}}}{I_{\mathrm{dark}}} \times 100 \tag{2}$$

wherein, I_{dark} and I_{p} are the dark and radiation currents.

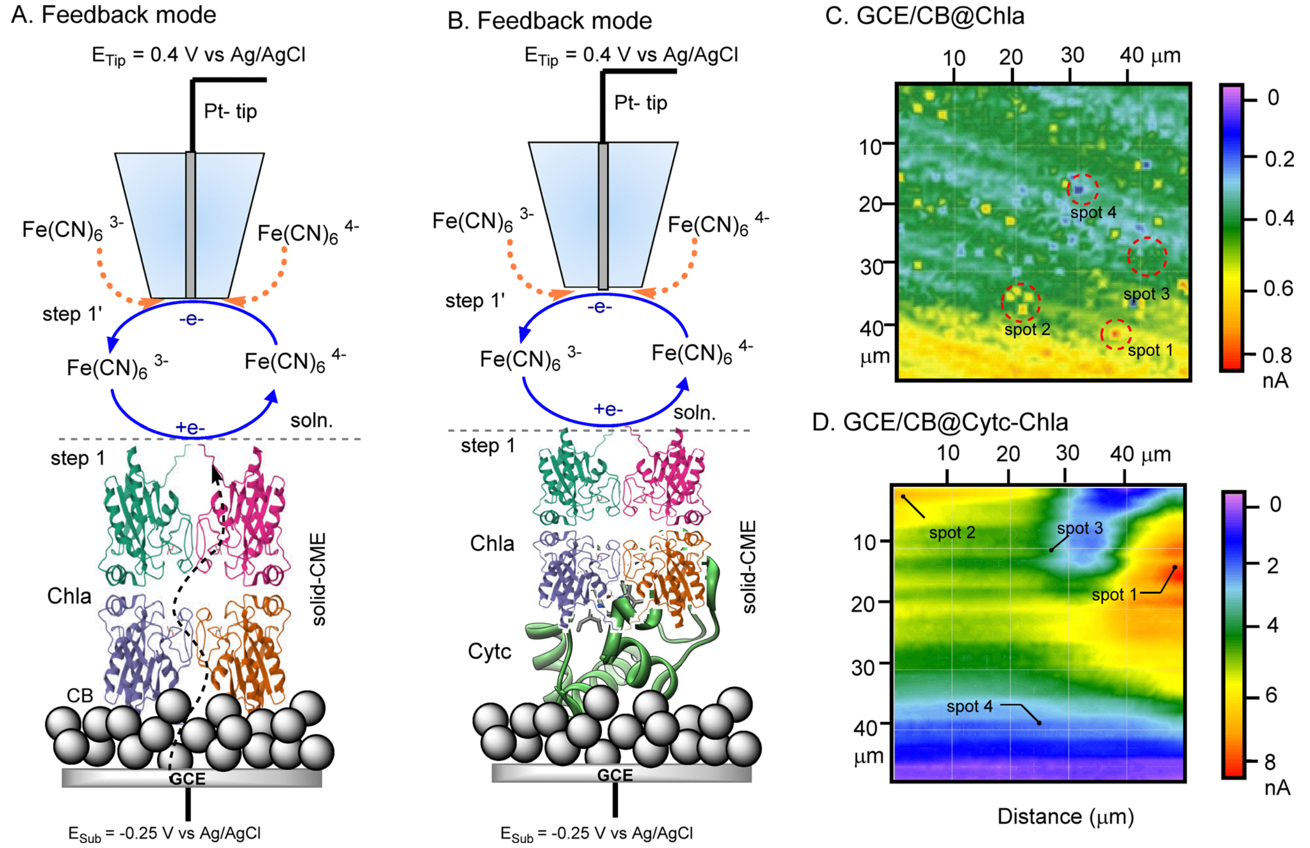

Fig. 5 (A) and (B) Schematic representation for the feedback current-based operation and mapping of the active site using the SECM technique, using 5 mM $Fe(CN)_6^{3-}$ containing N_2 purged 0.1 M KCl solution. SECM image of the (A) and (C) GCE/CB@Chl*a* and (B) and (D) GCE/CB@Cyt*c*–Chl*a* with various active spots. E_{Sub} = −0.25 V *vs.* Ag/AgCl and Pt_{Tip} = 0.4 V *vs.* Ag/AgCl.

In a nitrogen atmosphere, the SPE/CB (Fig. S7A; curve a) shows a feeble PC (∼0.1 μA cm^{-2}). Mostly low dimensional carbon nanomaterials (carbon nanotubes, quantum dots, graphene oxides, reduced graphene oxides, *etc.*) exist in PC due to various factors such as large specific surface areas and abundant surface states, which can be modulated by band engineering and trion formation (when an additional charge carrier (either an electron or a hole) joins to an existing exciton, forming a charged exciton complex).[59,60] Fig. 6A (curve a), represents the immobilization of Cyt*c* on CB (SPE/CB@Cyt*c*) (∼1.6 μA cm^{-2}), it shows a moderate PC response was observed due to various factors like trapping of charge carriers and recombination due to negative bias potential or Cyt*c* undergoes conformational changes upon illumination,[58–61] which can affect its electronic states. Similarly, Fig. 6A, curve b, of SPE/CB@Chl*a* (∼1.5 μA cm^{-2}) shows a relatively appreciable PC response with consistent behavior when compared to SPE/CB@Cyt*c*–Chl*a* (3 μA cm^{-2}). As a photoreceptor for visible light conversion, Chl*a* is one of the biological pigments or their model compounds, and it has become a key area of study in modern photoelectrochemistry. Chl*a* has attracted particular attention due to its strong electrochemical reactivity and benefit in harnessing the red portion of solar energy. Therefore, better charge transport can take place in the modified electrode through Chl*a*.[59,62] Meanwhile, as control experiments, the modified electrodes, SPE/CB@Cyt*c* and SPE/CB@Chl*a*, were coated with photo-inactive protein like BSA (Fig. S7, curves b and c), validating the photochemical reactivity of the biocomposite. Both the BSA-coated systems showed negligible photocurrent activities (<1 μA cm^{-2}), revealing the photo-insensitivity of the BSA on the overall photocurrent activity. Plausibly, BSA film might resist Chl*a* and Cyt*c* in structural conformational change under illumination by its insulating nature, which limits the light reaching the interface of the immobilization (Chl*a* or Cyt*c*).[63] Fig. 6A, curve c, for CB@Cyt*c*–Chl*a*, shows the highest values of 3 μA cm^{-2}, revealing the synergistic effect between Cyt*c* and Chl*a*. Due to its complementary roles, Chl*a* harvests light, and Cyt*c* ensures efficient charge transfer. Furthermore, the interactions between the Chl*a* and Cyt*c*, Chl*a* residues of Asp162, Asp163, Ser166, Glu168, and Asn169 have close interaction with cytochrome *c* (Thr28, Lys79, Ile81, and Ala83). Ser166 and Asn169 residues of Chl*a* exhibit hydrophobic interactions with Ala83, Ile81, and Thr28 of cytochrome *c*, as previously demonstrated by docking studies.

Those interactions and the electron shuttling between Chl*a* and Cyt*c* might form biomolecular cross linkages to enhance photoconductance under illumination. Fig. 6E shows the schematic representation of CB@Cyt*c*–Chl*a* under irradiation. The incident light generates an electron–hole pair, which can oxidize oxygen into oxygen radicals in pH 7 PBS, showing a

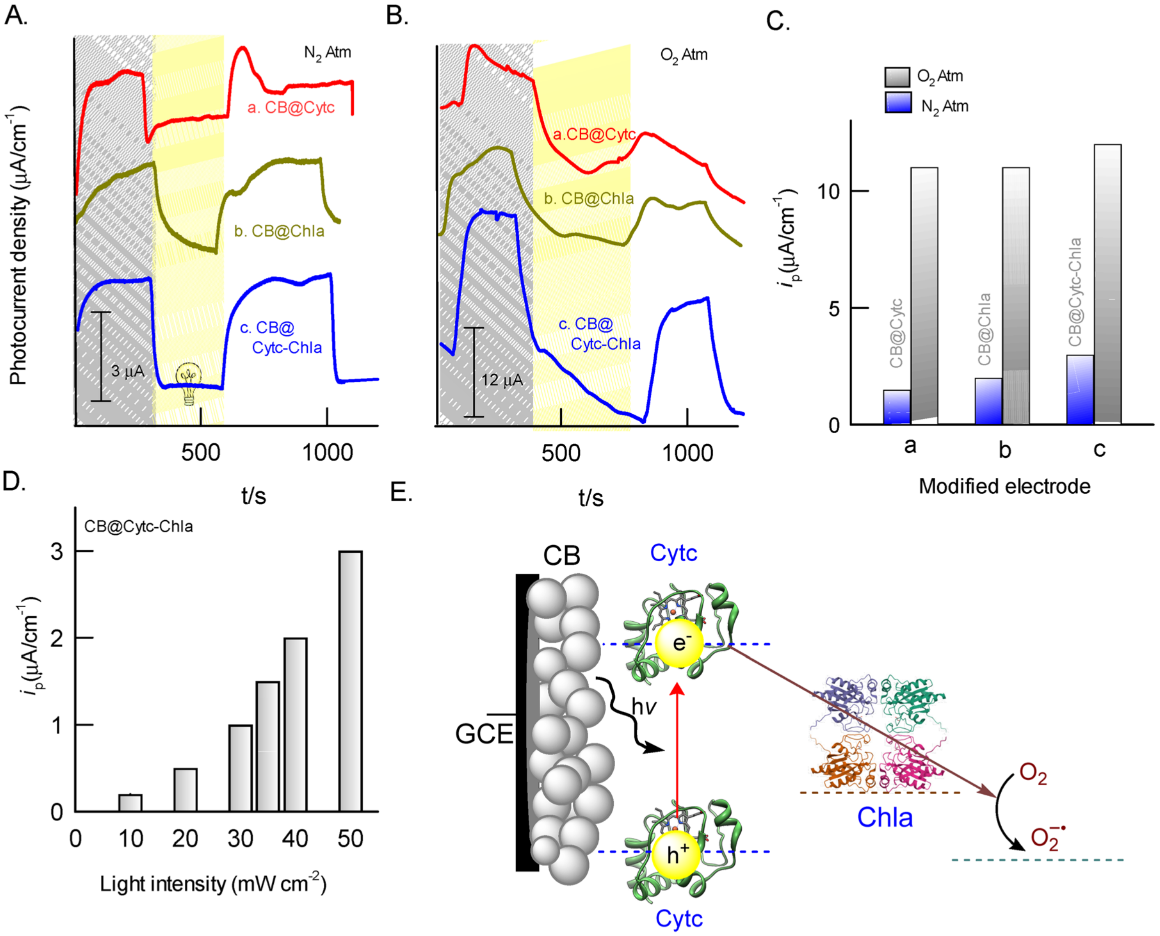

Fig. 6 (A) and (B) Photocurrent responses were recorded in amp-it at −0.25 V *vs.* Ag/AgCl of CB@Cytc (a), CB@Chl*a* (b) and CB@Cytc–Chl*a* (c) modified electrodes in pH 7 PBS-N_2 and O_2 atm. (C) i_p value of modified electrodes in different atmospheres. (D) i_p value of CB@Cytc–Chl*a* in different light intensities (10–50 mW cm^{-2}) and (E) schematic representation of CB@Cytc–Chl*a* under irradiation. The incident light generates an electron–hole pair, which can oxidize oxygen into oxygen radicals in pH 7 PBS.

plausible mechanism for the overall photocurrent activity. Fig. 6C and Fig. S7B reveal the actual current difference between the modified electrode in different atmospheres and different modifications. The increased photoconductance yield is mainly due to the interaction between the amino groups of Chl*a* with Cyt*c*. The decreased/lower photo-conductance yield in CB, CB@Cyt*c*, CB@Chl*a*, CB@Chl*a*/BSA, and CB@Cyt*c*/BSA may be due to the reduced surface-to-volume ratio for agglomeration, surface hindrances, and lack of interactions with the carbon surface. The photoconductance yield reaches a maximum for CB@Cyt*c*–Chl*a* (112%) and slightly decreases for CB@Cyt*c* (35%), CB@Chl*a* (34%), CB@Chl*a*/BSA (25%), CB@Cyt*c*/BSA (20%) and CB (7%) in a N_2 atmosphere. For comparison of the photo-conductance yield of the reported negative PC (NPC) materials, we have compared our results of CB@Cyt*c*–Chl*a* with the reported values for functionalized CNTs,[64] graphene,[65,66] and Au-silk protein.[58] The results are presented in Table 3. It is observed that the CB@Cyt*c*–Chl*a* exhibits the highest photoconductance yield as compared to the previously reported results. This indicates the superior properties of CB@Cyt*c*–Chl*a* over the inorganic NPC materials, as an active biomolecule for photonic applications.

Table 3 Comparison of CB@Cytc–Chl*a* photoconductance yields with previously reported similar materials, like carbon and proteins

Material	Photoconductance yield (%)	Ref.
1. PbS/MWCNT	∼31	64
2. Graphene	34	65
3. QDs/CNT	86	66
4. Au-silk protein	98	58
5. CB@Cyt*c*–Chl*a*	112	This work

Fig. S7C shows that the photocurrent responses at increasing light intensities (10–50 mW cm^{-2}) were examined, with CB@Cyt*c*–Chl*a* consistently displaying the highest photocurrent at each intensity level. The photocurrent is linearly dependent on the light intensity. The linear increase in photocurrent density with light intensity, as shown in Fig. 6D, suggests efficient charge separation and transfer processes facilitated by the Cyt*c*–Chl*a* complex. The trend implies potential applicability in scalable light-harvesting systems where variable light conditions are exposed.

3.6. Bio-electrocatalytic reduction of H_2O_2

In this study, H_2O_2 was employed as a model analyte to investigate the molecular wiring between Cyt*c* and Chl*a*.

Fig. 7A displays the comparative CV responses of various modified electrodes, including GCE/CB, GCE/CB@Cyt*c*, GCE/CB@Chl*a*, and GCE/CB@Cyt*c*–Chl*a*, recorded in a nitrogen-purged phosphate buffer solution (PBS, pH 7) containing 20 μM H_2O_2 (10 mL total volume). Poorly defined cathodic responses were observed at approximately −0.21 V *vs.* Ag/AgCl for both GCE/CB, with limited electrocatalytic activity. In contrast, GCE/CB@Chl*a* and GCE/CB@Cyt*c* exhibited moderate reduction peaks at −0.35 V and −0.17 V *vs.* Ag/AgCl, respectively. Notably, the GCE/CB@Cyt*c*–Chl*a* electrode demonstrated a well-defined reduction peak at −0.20 V *vs.* Ag/AgCl with a cathodic current nearly twice that of GCE/CB@Cyt*c* and GCE/CB@Chl*a*. Furthermore, as shown in Fig. 7B, the GCE/CB@Cyt*c*–Chl*a* electrode exhibited approximately a 30-fold enhancement in cathodic peak current compared to the unmodified GCE/CB electrode. This substantial increase highlights the efficient electrocatalytic reduction of H_2O_2 facilitated by the integrated Cyt*c*–Chl*a* system on the electrode surface.

To further investigate the electron transfer behavior, the effect of scan rate was studied for the GCE/CB@Chl*a*, GCE/CB@Cyt*c* and GCE/CB@Cyt*c*–Chl*a* electrode in the presence of 20 μM H_2O_2. As shown in Fig. 7C and Fig. S8(A and B), the current response increased progressively with the scan rate. A linear relationship was observed between the i_{pc} and the square root of the scan rate, starting from the origin up to 100 mV s^{-1}, indicating a diffusion-controlled electrochemical process (Fig. 7D and Fig. S8C). Fig. 7E and Fig. S8(D and E) depict the effect of varying H_2O_2 concentrations (5–40 μM) on the CV response of the GCE/CB@Cyt*c*–Chl*a*, GCE/CB@Chl*a* and GCE/CB@Cyt*c* electrode in N_2-purged phosphate buffer solution (PBS, pH 7). A sharp increase in current was observed with increasing H_2O_2 concentration up to 40 μM, beyond which the response plateaued, indicating saturation behavior as shown in Fig. 7F and Fig. S8F. The calculated current sensitivity was 0.903 μA μM^{-1}. This saturation trend is characteristic of Michaelis–Menten (MM) type enzymatic kinetics. The proposed reaction mechanism for the MM-type catalytic reduction of H_2O_2 at the CB@Cyt*c*–Chl*a*-modified electrode is illustrated in Scheme 3. Initially, H_2O_2 binds reversibly to the reduced form of cytochrome *c* (Cyt*c*-Fe^{2+}). This is followed by the catalytic reduction of H_2O_2, resulting in the oxidation of the protein to Cyt*c*-Fe^{3+}. The oxidized Cyt*c* is then electrochemically reduced back to its active form (Cyt*c*-Fe^{2+}) at the applied potential of −0.2 V *vs.* Ag/AgCl.

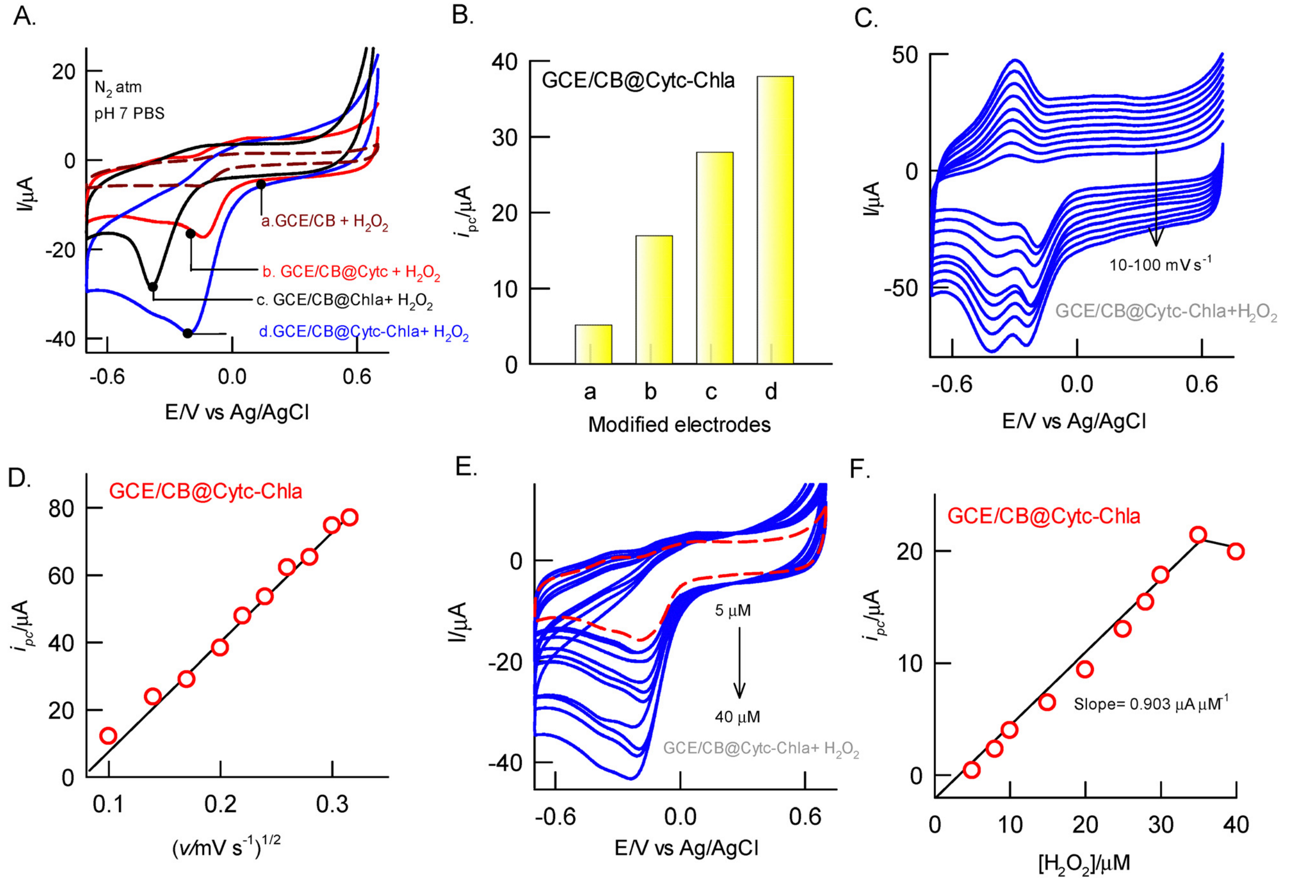

Fig. 7 (A) CV response of (a) GCE/CB, (b) GCE/CB@Cyt*c*, (c) GCE/CB@Chl*a* and (d) GCE/CB@Cyt*c*–Chl*a* with 20 μM of H_2O_2 in pH 7 PBS (N_2 purged). (B) A comparative plot of i_{pc} *vs.* different modified electrodes (a–d). (C) Effect of the scan rate of GCE/CB@Cyt*c*–Chl*a* in the presence of 20 μM of H_2O_2 in pH 7 PBS (N_2 purged). (D) Plot of the cathodic peak current i_{pc} *vs.* square root of *v*. (E) Effect of the concentration (5–40 μM) of H_2O_2 of GCE/CB@Cyt*c*–Chl*a* in pH 7 PBS (N_2 purged) and (F) plot of $|i_{pc}|$ *vs.* $[H_2O_2]$/(μM) (baseline corrected).

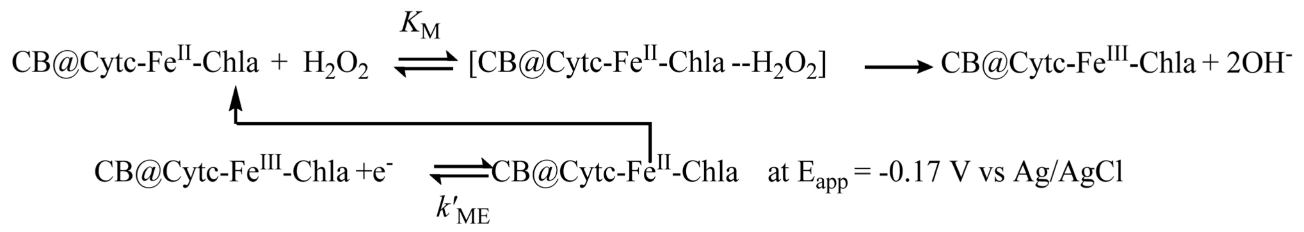

Scheme 3 Reaction route on the electrochemically mediated Michaelis–Menten (MM) type reaction kinetics of CB@Cytc–Chl*a* assisted reduction of H_2O_2 under electrochemical conditions.

3.7. Bio-electroanalytical performance of H_2O_2

As a practical application of the bioelectrode of SPE/CB@Cyt*c*–Chl*a*, batch injection analysis (BIA) combined with disposable screen-printed electrodes has been used (Fig. 8A). Significantly, BIA is a straightforward fluidic technique that makes it easier to analyze target analytes continuously and in small volumes (50 µL). BIA requires about 50 mL of static bulk electrolyte solution, whereas flow injection analysis (FIA) requires a peristaltic pump and a high-precision injector. Using a preprogrammed robot micropipette system, it can automatically spike the target analyte with volumes ranging from 20 to 200 µL, and the BIA setup photographic image is displayed in Fig. 8B. Before the electroanalysis, associated parameters for the H_2O_2 detection were individually tuned as 1 mm^3 s^{-1}, 50 µL, and $E_{app} = -0.17$ V, respectively; these parameters included stir rate, spike volume, and applied potential. Fig. 8A describes the typical BIA responses of CB@Chl*a* (curve a), CB@Cyt*c* (curve b), and CB@Cyt*c*–Chl*a* (curve c) for continuous spikes of H_2O_2 in a concentration range of 2 to 25 µM. The CB@Cyt*c*–Chl*a* electrode exhibited inconsistent current signals under similar conditions when compared with other systems, whereas the biomimetic electrode displayed a regular increase in the peak current with the rise in the H_2O_2 concentration.

The effect of interference was examined by conducting BIA in the presence of 10 µM of cysteine (CySH), dopamine (DA), glucose (Glu), iodide (I$^-$), urea, ascorbic acid (AA), uric acid (UA), adenine (Ade), and nicotinamide dinucleotide hydrogen (NADH) under optimal working conditions (Fig. 8C). No significant current response was obtained upon spiking of the above interferent biochemicals, underscoring the selective response of the biomimicking electrode toward H_2O_2 analysis.[58,64]

3.8. Wireless monitoring of ROS released by cells

As an extended analytical application, the CB@Cyt*c*–Chl*a* sensor, integrated into a three-in-one electrode assembly and connected to a portable wireless device, was employed as an electrochemical tool for real-time monitoring of reactive oxygen species (ROS) in biological samples. Fig. 8D schematically

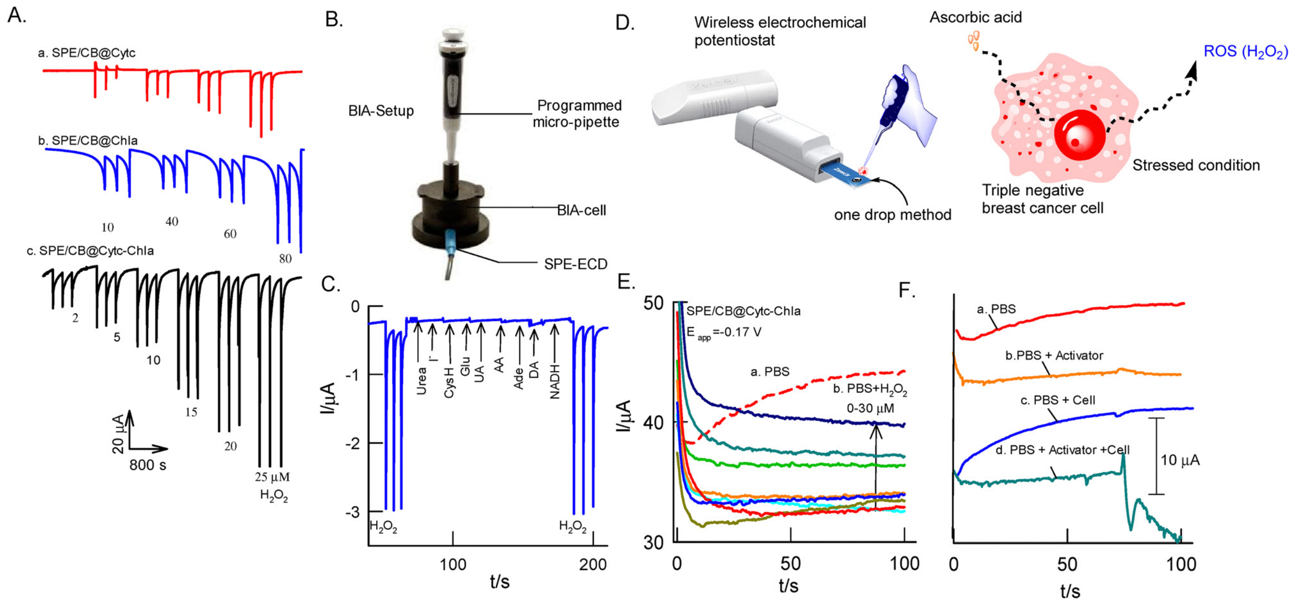

Fig. 8 (A) Typical BIA response of (a) GCE/CB@Cyt*c*, (b) GCE/CB@Chl*a*, and (c) GCE/CB@Cyt*c*–Chl*a* with gradual increasing of H_2O_2 in pH 7 PBS (N_2 purged) at the applied potential of −0.17 V *vs.* Ag/AgCl. (B) Photographic setup of BIA. (C) Interference effect of various bioactive chemicals of 10 µM of urea, iodide (I$^-$), cysteine (CysH), ascorbic acid (AA), uric acid (UA), glucose (Glu), adenine (Ade), dopamine (DA) and nicotinamide dinucleotide hydrogen (NADH). The wireless prototype Zensor (D) schematically represents the wireless prototype system, and the ROS detection from cancerous cells. Amp *i*–*t* response of (E) SPE/CB@Cyt*c*–Chl*a* on various concentrations of H_2O_2 and (F) triple-negative breast cancer cell detection with control experiments.

represents the wireless prototype system and the ROS detection response of the cancerous cells. The clear electrochemical differentiation between normal cancerous and stress-induced cell environments underscores its utility in identifying biochemical markers associated with oxidative stress. Initially, as shown in Fig. 8E, the SPE/CB@Cyt*c*–Chl*a* electrode was subjected to amperometric *i*–*t* measurements by applying 10 μL of the test electrolyte or analyte-dissolved solution onto the sensor electrode surface. As a control experiment, the sensor was tested with various concentrations of H_2O_2 (0 to 30 μM) *via* drop-casting 10 μL aliquots directly onto the sensor electrode surface. The resulting amperometric response (Fig. 8E) displayed a good linear correlation between the H_2O_2 concentration and the corresponding current signal, confirming the sensor's sensitivity and reliability for peroxide detection. Fig. 8F illustrates the ROS monitoring capability of the SPE/CB@Cyt*c*–Chl*a* sensor in cancer cell environments. Before real sample analysis, several control samples – including phosphate-buffered saline (PBS), PBS containing ascorbic acid (AA, as an activator), and PBS with cancer cells – were tested by drop-casting on the electrode surface.

These control experiments showed negligible current responses, indicating the absence of ROS generation under those conditions. Interestingly, a marked increase in the reduction current was observed when the electrode was exposed to PBS containing both AA and cancer cells. This significant current enhancement suggests ROS formation at the sensor surface, particularly through the electrochemical reduction of intermediate ROS species such as H_2O_2. This observation highlights the sensor's capability to detect ROS in a biological context and supports its potential application in cancer diagnostics and biomedical research.

4. Conclusions

A molecularly wired bioelectrode comprising cytochrome *c* (Cyt*c*) and photosystem I (Chl*a*) proteins immobilized on a carbon black (CB)-modified electrode surface (denoted as CB@Cyt*c*–Chl*a*) was successfully fabricated using a simple drop-casting method followed by electrochemical treatments. The resulting bioelectrode exhibited a well-defined and reversible redox peak at a standard electrode potential of $E^\circ = -0.2$ V *vs.* Ag/AgCl in nitrogen-purged phosphate buffer solution (pH 7), indicative of efficient electron transfer. Control experiments, in which either cytochrome *c* or Chl*a* was individually immobilized onto the CB surface, failed to exhibit such redox behavior, confirming the essential role of cooperative interaction between the two proteins in facilitating the electron transfer process. The biochemical affinity between cytochrome *c* and Chl*a* was further investigated using *in situ* electrochemical quartz crystal microbalance (EQCM). Upon exposure of a gold crystal modified with CB@Cyt*c* to a dilute Chl*a* solution, a significant negative frequency shift was observed, confirming successful protein–protein interaction. In contrast, control setups lacking one of the components did not show notable frequency changes. Surface morphology and protein distribution on the electrode were visualized using *in situ* scanning electrochemical microscopy (SECM) in feedback mode. The imaging revealed a continuous, cloud-like molecular matrix, characteristic of a homogeneously distributed protein network exhibiting high electrochemical activity. Functionally, the CB@Cyt*c*–Chl*a* bioelectrode demonstrated significantly enhanced photocurrent under simulated solar illumination compared to electrodes modified with individual proteins. This enhancement is attributed to the photoexcited electron quenching of Chl*a* by cytochrome *c* and dissolved oxygen, supporting the proposed photoinduced electron transfer mechanism. Further validation of the molecular wiring was achieved through hydrogen peroxide (H_2O_2) reduction studies in a pH 7 buffer, where the hybrid system displayed a markedly higher reduction current compared to electrodes modified with either protein alone. This property was successfully utilized for bioelectroanalytical applications, including sensitive H_2O_2 detection using a disposable screen-printed electrode integrated with a batch injection analysis system, and reactive oxygen species (ROS) monitoring in chemically stressed cancer cells using a one-drop, wireless electrochemical detection method. Overall, the biomimetic CB@Cyt*c*–Chl*a* system developed in this work represents a robust, real-time functional model for solar-energy conversion, redox sensing, and biomedical diagnostics, with promising potential for a wide range of practical applications.

Author contributions

Jayaprakash Meena: investigation, formal analysis, resources, methodology, validation, data curation, visualization, writing-draft; Sugumar Monisha: investigation, formal analysis, resources, validation, data curation, visualization. Tamizhselvi Ramasamy: review, editing of cancer cell part. Kandhan Palanisamy: docking studies, formal analysis. Varatharaj Rajapandian: docking studies, formal analysis, visualization and writing of docking studies. K. Santhakumar: conceptualization, visualization, supervision; Annamalai Senthil Kumar: conceptualization, methodology, writing – original draft, writing – review & editing, visualization, supervision, project administration, funding acquisition.

Conflicts of interest

We wish to confirm that there are no known conflicts of interest associated with this publication and there has been no significant.

Data availability

The data supporting this article have been included as part of the supplementary information (SI). Supplementary information: effect of loading; CV response of porphyrin; AFM height measurement; selected top 3 docking conformation of Chl*a* and Cyt*c*; SECM $Fe(CN)_6^{3-/4-}$ CV responses and approach curves, scan rate effects, control concentration effects, and photocurrent response. See DOI: https://doi.org/10.1039/d5cp04355g.

Acknowledgements

The authors gratefully acknowledge the financial support of the Department of Science and Technology – Science and Engineering Research Board (DST–SERB), India, under the Core Research Grant Scheme (CRG/2021/001048).

References

1 A. F. Janzen and M. Seibert, *Nature*, 1980, **286**, 584–585.
2 R. Sobotka, H. J. Esson, P. Koník, E. Trsková, L. Moravcová, A. Horák, P. Dufková and M. Oborník, *Sci. Rep.*, 2017, **7**, 13214.
3 A. Tiwari, F. Mamedov, D. Fitzpatrick, S. Gunell, M. Tikkanen and E.-M. Aro, *Nat. Plants*, 2024, **10**, 1592–1603.
4 P. R. Chitnis, *Annu. Rev. Plant Physiol. Plant Mol. Biol.*, 2001, **52**, 593–626.
5 K. Brettel and W. Leibl, *Biochim. Biophys. Acta, Bioenerg.*, 2001, **1507**, 100–114.
6 Z. Wang, Y. Hu, S. Zhang and Y. Sun, *Chem. Soc. Rev.*, 2022, **51**, 6704–6737.
7 Y. Liu, A. Bin Mohamad Annuar, S. Rodríguez-Jiménez, C. W. S. Yeung, Q. Wang, A. M. Coito, R. R. Manuel, I. A. C. Pereira and E. Reisner, *J. Am. Chem. Soc.*, 2024, **146**, 29865–29876.
8 D. Mersch, C.-Y. Lee, J. Z. Zhang, K. Brinkert, J. C. Fontecilla-Camps, A. W. Rutherford and E. Reisner, *J. Am. Chem. Soc.*, 2015, **137**, 8541–8549.
9 B. Ghosh, *Emerg. Top Life Sci.*, 2022, **6**, 619–627.
10 R. Mandal and G. Dutta, *Sens. Int.*, 2020, **1**, 100058.
11 A. Machín, M. Cotto, J. Ducongé and F. Márquez, *Biomimetics*, 2023, **8**, 298.
12 H. A. Kalpage, J. Wan, P. T. Morse, M. P. Zurek, A. A. Turner, A. Khobeir, N. Yazdi, L. Hakim, J. Liu, A. Vaishnav, T. H. Sanderson, M.-A. Recanati, L. I. Grossman, I. Lee, B. F. P. Edwards and M. Hüttemann, *Int. J. Biochem. Cell Biol.*, 2020, **121**, 105704.
13 S. Zaidi, Md. I. Hassan, A. Islam and F. Ahmad, *Cell. Mol. Life Sci.*, 2014, **71**, 229–255.
14 F. M. Reyes-Sosa, J. Gil-Martínez and F. P. Molina-Heredia, *Photosynth. Res.*, 2011, **110**, 61–72.
15 R. G. Kranz, C. Richard-Fogal, J.-S. Taylor and E. R. Frawley, *Microbiol. Mol. Biol. Rev.*, 2009, **73**, 510–528.
16 S. Shcolnick and N. Keren, *Plant Physiol.*, 2006, **141**, 805–810.
17 I. McConnell, G. Li and G. W. Brudvig, *Chem. Biol.*, 2010, **17**, 434–447.
18 E. S. Andreiadis, M. Chavarot-Kerlidou, M. Fontecave and V. Artero, *Photochem. Photobiol.*, 2011, **87**, 946–964.
19 Y.-D. Yang, Q. Zhang, L. Khrouz, C. V. Chau, J. Yang, Y. Wang, C. Bucher, G. Henkelman, H.-Y. Gong and J. L. Sessler, *ACS Cent. Sci.*, 2024, **10**, 1148–1155.
20 O. Kievit and G. W. Brudvig, *J. Electroanal. Chem.*, 2001, **497**, 139–149.
21 G. LeBlanc, K. M. Winter, W. B. Crosby, G. K. Jennings and D. E. Cliffel, *Adv. Energy Mater.*, 2014, **4**, 1301953.
22 L. Than, K. D. Wolfe, D. E. Cliffel and G. K. Jennings, *Photosynth. Res.*, 2023, **155**, 299–308.
23 P. N. Ciesielski, A. M. Scott, C. J. Faulkner, B. J. Berron, D. E. Cliffel and G. K. Jennings, *ACS Nano*, 2008, **2**, 2465–2472.
24 L. A. Khanova and M. R. Tarasevich, *J. Electroanal. Chem. Interfacial Electrochem.*, 1987, **227**, 99–114.
25 M. Kato, T. Cardona, A. W. Rutherford and E. Reisner, *J. Am. Chem. Soc.*, 2013, **135**, 10610–10613.
26 S. C. Feifel, K. R. Stieger, H. Lokstein, H. Lux and F. Lisdat, *J. Mater. Chem. A*, 2015, **3**, 12188–12196.
27 S.-Y. Chen, Y.-Y. Lu, F.-Y. Shih, P.-H. Ho, Y.-F. Chen, C.-W. Chen, Y.-T. Chen and W.-H. Wang, *Carbon*, 2013, **63**, 23–29.
28 D. Das, J. Sarkar Manna and M. K. Mitra, *J. Phys. Chem. C*, 2015, **119**, 6939–6946.
29 B. Munge, S. K. Das, R. Ilagan, Z. Pendon, J. Yang, H. A. Frank and J. F. Rusling, *J. Am. Chem. Soc.*, 2003, **125**, 12457–12463.
30 V. Proux-Delrouyre, C. Demaille, W. Leibl, P. Sétif, H. Bottin and C. Bourdillon, *J. Am. Chem. Soc.*, 2003, **125**, 13686–13692.
31 M. Ciobanu, H. A. Kincaid, V. Lo, A. D. Dukes, G. Kane Jennings and D. E. Cliffel, *J. Electroanal. Chem.*, 2007, **599**, 72–78.
32 P. N. Ciesielski, A. M. Scott, C. J. Faulkner, B. J. Berron, D. E. Cliffel and G. K. Jennings, *ACS Nano*, 2008, **2**, 2465–2472.
33 T. Bennett, H. Niroomand, R. Pamu, I. Ivanov, D. Mukherjee and B. Khomami, *Phys. Chem. Chem. Phys.*, 2016, **18**, 8512–8521.
34 S. Tanimoto and A. Ichimura, *J. Chem. Educ.*, 2013, **90**, 778–781.
35 T. Kawawaki, Y. Negishi and H. Kawasaki, *Nanoscale Adv.*, 2020, **2**, 17–36.
36 N. Torabi, X. Qiu, M. López-Ortiz, M. Loznik, A. Herrmann, A. Kermanpur, A. Ashrafi and R. C. Chiechi, *Langmuir*, 2021, **37**, 11465–11473.
37 J. Sławski, J. Maciejewski, R. Szukiewicz, K. Gieczewska and J. Grzyb, *ACS Omega*, 2023, **8**, 41991–42003.
38 P. N. Ciesielski, C. J. Faulkner, M. T. Irwin, J. M. Gregory, N. H. Tolk, D. E. Cliffel and G. K. Jennings, *Adv. Funct. Mater.*, 2010, **20**, 4048–4054.
39 M. J. Allen, V. C. Tung and R. B. Kaner, *Chem. Rev.*, 2010, **110**, 132–145.
40 D. Chen, H. Feng and J. Li, *Chem. Rev.*, 2012, **112**, 6027–6053.
41 M. Jerigová, M. Odziomek and N. López-Salas, *ACS Omega*, 2022, **7**, 11544–11554.
42 L. M. González, D. Ramirez and F. Jaramillo, *J. Energy Chem.*, 2022, **68**, 222–246.
43 X. Lu, G. J. Lian, J. Parker, R. Ge, M. K. Sadan, R. M. Smith and D. Cumming, *J. Power Sources*, 2024, **592**, 233916.
44 T. A. Silva, F. C. Moraes, B. C. Janegitz and O. Fatibello-Filho, *J. Nanomater.*, 2017, **2017**, 1–14.

45 Y. Wang, H. Feng, H. Zhang, Y. Chen, W. Huang, J. Zhang, X. Jiang, M. Wang, H. Jiang and X. Wang, *Analyst*, 2020, **145**, 1294–1301.

46 J. Jiao, L. Wen, Z. Wang, B. Han, L. Zhao and Q. Chen, *J. Electrochem. Soc.*, 2020, **167**, 067524.

47 S. Srinivas, N. Sivakumar, M. Sekar, K. Thirumurugan and A. Senthil Kumar, *J. Mater. Chem. C*, 2024, **12**, 11885–11897.

48 D. Horigome, H. Satoh, N. Itoh, K. Mitsunaga, I. Oonishi, A. Nakagawa and A. Uchida, *J. Biol. Chem.*, 2007, **282**, 6525–6531.

49 G. W. Bushnell, G. V. Louie and G. D. Brayer, *J. Mol. Biol.*, 1990, **214**, 585–595.

50 B. Jiménez-García, C. Pons and J. Fernández-Recio, *Bioinformatics*, 2013, **29**, 1698–1699.

51 W. Humphrey, A. Dalke and K. Schulten, VMD: Visual Molecular Dynamics, 1996.

52 V. Y. Lunin, A. Urzhumtsev, A. Bockmayr, A. Fokin, A. Urzhumtsev, P. Afonine, V. Y. Lunin, M. Harding, M. Turkenburg, C. Ballard and M. Howard-Eales, Theory and Techniques 12. Binary Integer Programming and its Use for Envelope Determination Bulk Solvent Correction for Yet Unsolved Structures Search of the Optimal Strategy for Refinement of Atomic Models Metal Coordination Groups in Proteins: Some Comments on Geometry, Constitution and B-values.

53 V. Lavanya, D. Pavithra, A. Mohanapriya, K. Santhakumar and A. Senthil Kumar, *Langmuir*, 2023, **39**, 11556–11570.

54 M. Gandhi, D. Rajagopal and A. Senthil Kumar, *Electrochim. Acta*, 2021, **368**, 137596.

55 S. Monisha, M. Subhashria, K. S. S. Devi, V. Manju and A. S. Kumar, *Electrochim. Acta*, 2024, 144515.

56 S. Monisha, A. Mary Saral and A. Senthil Kumar, *J. Electroanal. Chem.*, 2021, **901**, 115757.

57 S. Srinivas and A. Senthil Kumar, *Langmuir*, 2024, **40**, 10634–10647.

58 N. Gogurla, A. K. Sinha, D. Naskar, S. C. Kundu and S. K. Ray, *Nanoscale*, 2016, **8**, 7695–7703.

59 N. K. Tailor, C. A. Aranda, M. Saliba and S. Satapathi, *ACS Mater. Lett.*, 2022, **4**, 2298–2320.

60 B. Cui, Y. Xing, K. Niu, J. Han, H. Ma, W. Lv, T. Lei, B. Wang and Z. Zeng, *J. Sci.:Adv. Mater. Devices*, 2022, **7**, 100484.

61 Y. Agam and N. Amdursky, *J. Phys. Chem. C*, 2023, **127**, 17939–17947.

62 Z. Salamon and G. Tollin, *Photochem. Photobiol.*, 1993, **58**, 730–736.

63 R. Wang, X. Zhou, X. Zhu, C. Yang, L. Liu and H. Shi, *ACS Sens.*, 2017, **2**, 257–262.

64 W. Feng, C. Qin, Y. Shen, Y. Li, W. Luo, H. An and Y. Feng, *Sci. Rep.*, 2014, **4**, 3777.

65 C. Biswas, F. Güneş, D. D. Loc, S. C. Lim, M. S. Jeong, D. Pribat and Y. H. Lee, *Nano Lett.*, 2011, **11**, 4682–4687.

66 C. Biswas, H. Jeong, M. S. Jeong, W. J. Yu, D. Pribat and Y. H. Lee, *Adv. Funct. Mater.*, 2013, **23**, 3653–3660.